Characterization and optimization of Silicon Photomultipliers and small size scintillator tiles for future calorimeter applications

László Varga

Faculty of Science

Eötvös Loránd University, HU

Supervisor: Dr. Eva Sicking
Consultant: Dr. Ákos Horváth

A thesis submitted for the degree of

Master of Physics

Budapest 2017

Abstract

For the active layers of highly granular sampling calorimeters, small scintillator tiles read out by Silicon Photomultipliers (SiPM) can be an interesting and cost effective alternative to silicon sensors. At CERN a test setup was realized for the development of new generations of calorimeters to characterize new types of Silicon Photomultipliers in terms of gain, noise, afterpulses and crosstalk and to study the impact of scintillator wrappings and the tile size on the measured light yield and uniformity. In this thesis work, the experimental setup is described and the steps for commissioning the equipment are discussed. Then, the temperature dependence of the Silicon Photomultiplier response will be investigated, including the dependence of bare Silicon Photomultipliers as well as Silicon Photomultipliers coupled to scintillator tiles. Finally, the tile-photomultiplier response for different tile sizes and coating options will be evaluated. The experimental setup will be extended to allow for the characterization of the uniformity and the inter-tile crosstalk in multi-tile setups including two and four tiles.

Contents

Chapter 1

Introduction

The thesis describes detector research and development for highly granular sampling calorimeters for experiments at future e^+e^- colliders such as the Compact Linear Collider (CLIC). As one of the options for the calorimeter's active material, layers of small-size plastic scintillator tiles with silicon photomultiplier (SiPM) read out are investigated. Within the Linear Collider Detector (LCD) group at CERN, an experimental test bench was developed to characterize the scintillator tiles and SiPM. First, the working principle of the SiPM and the scintillator tiles are introduced together with their measurement setups for gain calibration and for scintillator tile scans, taking into account the measurement methods and the measured quantities. Then, the SiPM is characterized by measuring the breakdown voltage. Then it is calibrated including the overvoltage calibration, the temperature dependence on the intrinsic gain and on the collected charge recorded in scintillator tile scans. After that, using the calibrated SiPM response, data from scintillator tile scans are analyzed in order to study the light yield and the uniformity of the response for different tile sizes and coatings. Finally, an outlook including suggestions for additional multi-tile measurements is given.

Chapter 2

The Compact Linear Collider

The Compact Linear Collider (CLIC) is a concept for a future e^+e^- collider with center-of-mass energies ranging from a few hundred GeV up to 3 TeV [1]. When the electron and the positron interact in the collision annihilation occurs, liberating all their energy for the production of new particles. Both can be considered as point sized particles, therefore the reconstruction of the interaction process is more simple than for hadrons. In addition, as in CLIC fermions collide with antifermions, it provides complementary information to the LHC. The collider will be built in stages with different objectives. The first stage will be at 380 GeV. One of the main goals is to measure the Higgs properties with excellent accuracy to better understand the relation between the Higgs field and matter. Also the top quark can be studied in this stage. The second and third stages are currently being designed for 1.5 TeV and 3 TeV in order to study phenomena beyond the Standard Model. The energy stages can however be adjusted in case of discoveries at the LHC and at CLIC. The construction of the CLIC accelerator could start around 2025, the comissioning of CLIC would then take place around 2035 [1].

2.1 Overview of the CLIC accelerator complex

The layout of the CLIC accelerator complex at 3 TeV is shown in Figure 2.1 and its working principle is discussed in details in the CLIC CDR [2]. Its working mechanism is based on the use of two beams. The so-called Main Beams, of which particles take part in the collision, are accelerated by the so-called Drive Beam. The working mechanism is the following: The two Main Beams are generated at the e^+e^- injectors and pre-accelerated in the injector linacs. For beam emittance reduction the beams are transported through Damping Rings (DR). Then a further acceleration is made by the booster linac, and the beams are sent to the turn-arounds. After the turn-arounds

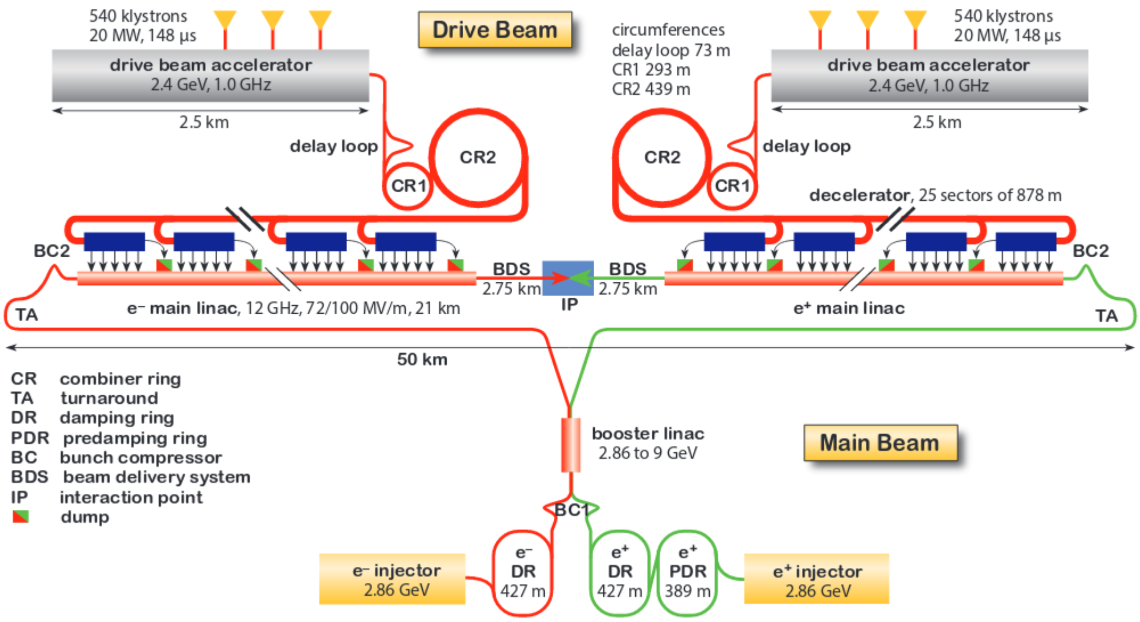

Figure 2.1: Layout of the 3 TeV CLIC accelerator complex [1].

the Main Beam is accelerated in RF cavities with a gradient of 100 MV/m. For this, instead of klystron powering, a second particle beam is used, the Drive Beam, which is decelerated and its kinetic energy is reconverted into radio frequency (RF) power. The Drive Beam is generated in two Main Linacs and the pulses of the Drive Beam are successive time compressed in the Delay Loops (DL) and Combiner Rings (CR1 and CR2). This compressed Drive Beam travels through the Main Linac tunnel to many individual turn-arounds, where each segment of the Drive Beam is sent through power extraction structures for RF power generation for the acceleration of the Main Beam. After the acceleration with the RF power extracted from the Drive Beam, the Main Beam is focused in the Beam Delivery System (BDS) and collides in the interaction point (IP) in the center of the CLIC detector.

2.2 CLIC detector

The physics program at CLIC focuses on the precision measurements of the Standard Model of particle physics such as on Higgs and top quark physics and the exploration and understanding of New Physics phenomena beyond the Standard Model [3]. Therefore, the requirements on the detector performance include precise momentum resolution and vertex reconstruction as well as distinguished particle identification. The CLIC detector (CLICdet) is barrel shaped and follows the structure of modern

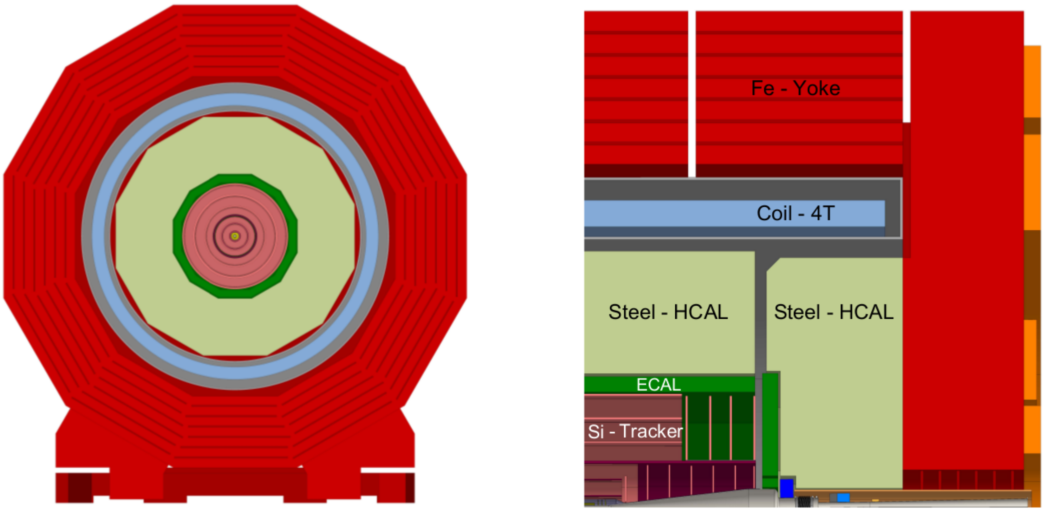

Figure 2.2: Left panel: The transverse cross section of the CLICdet [4]. Right panel: A quarter of the longitudinal cross section of the CLICdet model [4]. The overall dimensions of the detector are ⌀12.9 m in diameter and 11.4 m in length. The full detector has a weight of 8100 t.

particle detectors. The innermost layers are the tracking layers, such as the vertex detector and the silicon tracker, to measure the trajectory of the traversing charged particles. The tracker is followed by electromagnetic and hadronic calorimeters. The calorimeters measure the energy of the particles due to absorption. The next element of the detector is the superconducting magnet that generates a magnetic field of 4 T allowing precize measurement of particle momenta. The outermost layers are made of iron, on the one hand to identify the muons and on the other hand to return the magnetic flux to the detector solenoid. Moreover, in the forward region additional electromagnetic calorimeters measure the luminosity.

In the following, the CLICdet detector model will be described based on [4].

2.2.1 The vertex detector

The vertex detector consists of 3 double barrel layers and it is closed off in forward direction by disks. Both the barrel layers and the disks has a double-walled structure. The vertex detector is cooled by a spirally guided air-flow from outside to the center of the detector realized by spiral-shaped end caps in the forward region. The smallest inner radius is 31 mm, the length of the barrel is 260 mm. The vertex detector is made from $25 \times 25\ \mu m^2$ pixels which have analog readout allowing to read a position resolution of $3\ \mu m$. The technology is subject of ongoing pixel detector research and development (R&D) studies within the CLIC detector and physics (CLICdp) collaboration.

2.2.2 The silicon tracker

The CLICdet has an all-silicon tracker system. The whole tracking volume has a radius of 1.5 m with 4.4 m length. For installation and maintenance reasons, the tracker system is divided by the support tube into an "inner" (marked with dark-red color in Figure 2.2) and an "outer" (marked with dark-green color in Figure 2.2) tracker region. The Inner Tracker contains 3 barrel layers and seven inner tracker disks on each side of the barrel. The Outer Tracker contains three large barrel layers with four outer tracker disks on each sides of the barrel. All tracker layer's basic unit is the module. The outer tracker disks are assembled from the same type of modules with size of $30 \times 30\,\mathrm{mm}^2$, the inner tracker disks are made of modules with $15 \times 15\,\mathrm{mm}^2$ sensors. The modules are arranged into a larger group called petal. The petals have a small overlap in radial direction in all tracker disks, but no overlap along the detector axis. Details of the layout can be found in [5].

2.2.3 Particle flow calorimeter

The tracking detectors of the CLIC detector are followed first by the electromagnetic sampling calorimeter (ECAL), then by the hadronic sampling calorimeter (HCAL) that follow the principle of particle flow. The particle flow analysis (PFA) is a new approach for calorimetry. Using PFA techniques, the jet energy resolution can be improved, with the goal to reconstruct the energies of the individual particles in a jet [6]. It requires highly segmented detectors combined with sophisticated reconstruction software. The average jet composition contains 60% charged particles, 30% photons and 10% neutral hadrons [7]. In PFA these components becomes separated as shown in Figure 2.3. The energies of the charged particle are well measured from the associated track momentum and the calorimeters are only used for the neutral electromagnetic and hadronic components. This technique has the ability to reach $3\% - 4\%$ jet energy resolution when using ECAL cell size $\sim 1 \times 1\,\mathrm{cm}^2$ (Figure 2.4) [8].

Preliminary cost estimates of the CLIC detector showed that an electromagnetic calorimeter (ECAL) based on silicon sensors is one of the major cost drivers [4]. However, scintillator tiles are a possible cost-saving alternative to silicon as active

Figure 2.3: The separation of the jet components are made by the reconstruction software using the informations of the tracker and vertex detector and the highly granular calorimeters [9].

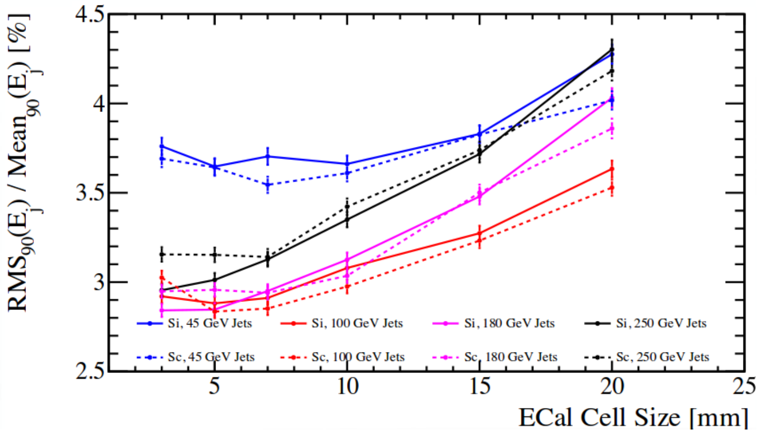

Figure 2.4: The jet energy resolution as function of the ECAL cell size significantly decreases for smaller tile sizes for both the silicon and scintillator ECAL models [8].

material. For the CLICdet a silicon-tungsten ECAL with 40 layers is chosen, which contains 1.9 mm thick tungsten absorber plates with silicon sensor cells of $5 \times 5\,\text{mm}^2$. The silicon sensors have a thickness of 0.5 mm. The HCAL consists of 60 layers with 19 mm thick absorber plates with scintillator cells of $3 \times 3\text{mm}^2$ read out by Silicon Photomultipliers as active material unit. The scintillator has a thickness of 3 mm.

The HCAL has a depth of 7.5 λ_I in both the endcap and the barrel.

2.2.4 Magnet system

The magnet system of the CLICdet model consists of a superconducting solenoid with a 3-module coil which produces a field of 4 T in the center of the detector. In addition, it consists a steel return yoke with three barrel yokes and two end caps completed with end coils. With the usage of the end coils the thickness of the yoke end caps can be reduced.

2.2.5 Muon system and yoke

In the CLICdet model, the iron return yoke is used as muon identifier. The muon system design is guided by the requirements on the yoke, which returns the magnetic flux to the detector solenoid. The iron return yoke is structured into three rings in the barrel region, and into two end caps with 6 muon detection layers distributed with equal space. The muon detection layers are planned to consist of resistive plate chambers (RPC) with cells of $30 \times 30\,\text{mm}^2$ [4].

2.2.6 Forward system

The two main elements of the very forward region are two smaller electromagnetic sampling calorimeters, named LumiCal and BeamCal, improving the hermeticity of the detector. Both are aligned with the outgoing beam axis and provide coverage for re- constructing electrons and photons with very small angles. The LumiCal with its 40 layers is intended as a precise luminosity monitor. Each layer consists of 3.5 mm tungsten and 0.32 mm silicon sensors. Similarly, the BeamCal also contains 40 layers of 3.5 mm tungsten plates and completes the coverage of the electromagnetic calorimeter. As active material 0.3 mm thick diamond layers are currently investigated, which could be sufficiently radiation hard.

Chapter 3

The experimental setups for SiPM and scintillator characterization

In order to improve our understanding of scintillators and SiPMs and their related systematic effects in scintillator-based ECAL and HCAL applications, two experimental setups were commissioned by the Linear Collider Detector group at CERN. The first setup serves the purpose of scintillator characterization with different sizes and coatings as well as the better understanding of the uniformity of the measured light yield and the edge effects between several tiles. The second setup gives the possibility to investigate SiPMs, including their intrinsic amplification as a function of the temperature and as a function of the overvoltage as well as their related systematic effects.

This chapter provides first an overview of the working principle of the SiPMs and the scintillator tiles, then the above-mentioned setups will be introduced.

3.1 The working principle of an SiPM

SiPMs are single-photon sensitive devices consisting of an avalanche photodiode (APD) array on a common silicon substrate. The photodiode is an opto-semiconductor device, which generates current when photons are absorbed in it. The devices are widely used for Medical Imaging applications (for instance Position emission tomography (PET)) as well as for the detection of Cherenkov light. The popularity can be explained by their compactness, robustness, the insensitivity to magnetic fields and cost effectiveness. Due to the exploitation of the avalanche effect, the devices provide a high intrinsic amplification.

The study of different SiPMs was done, however, it would go beyond the scope of this thesis to discuss the analysis of these data, too. In this thesis, a Hamamatsu

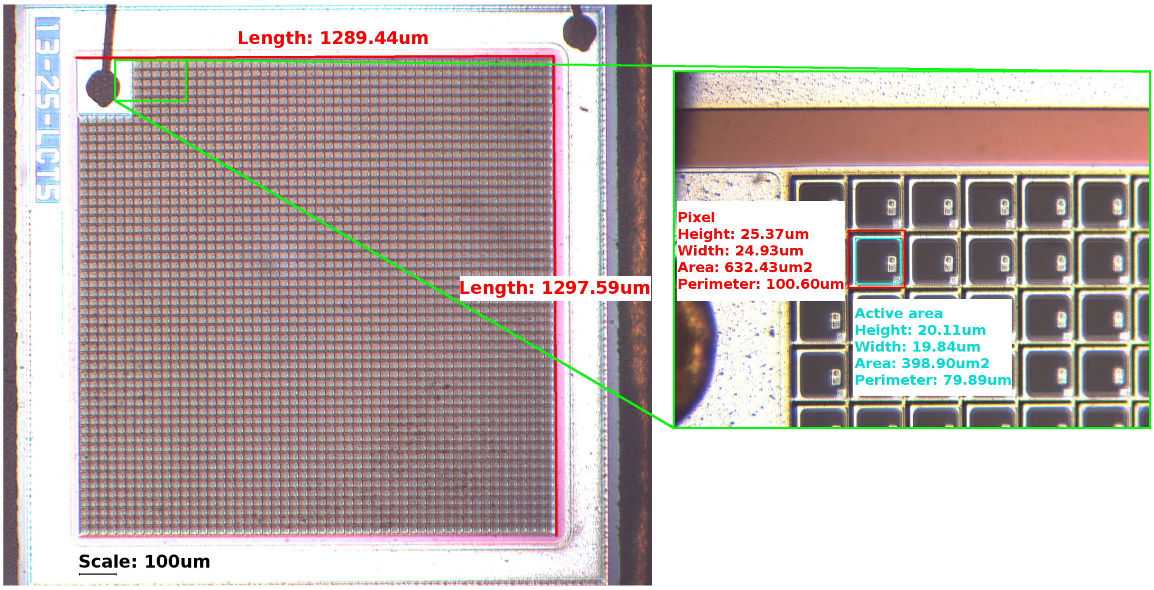

Figure 3.1: Magnified pictures of SiPM from Hamamatsu (type S13360-1325PE and some of its avalanche photo diodes. The active area compared to the total area of an APD is aprroximated 60%.

multi-pixel photon counter (MPPC is one of the devices named SiPM) type of the series S13360-1325PE is used. This MPPC with $1.3 \times 1.3\,\mathrm{mm}^2$ active area, 2668 pixels of 25 µm pixel pitch size is shown in Figure 3.1. The working principle of an SiPM is the following (see in Figure 3.2):
A bias voltage is applied to all APD creating a depletion zone of a high electric field. The diodes are reverse biased with a voltage above the breakdown voltage. If a photon reaches an APD it can create an electron-hole pair that is accelerated in the high electric field and thereby generate an ionization avalanche. Since the APDs are operated in Geiger mode, the efficiency of the single photon detection is high. On the other hand in Geiger mode, an APD represents a binary device so that the output signal is independent of the number of incident photons on one APD. To obtain a signal approximately proportional to the number of photons, many APD cells are arranged in an array. Each APD cell is connected through an individual quenching resistor $\mathrm{R_Q}$ to a common read out. These quenching resistors are necessary to cease the Geiger discharge.

After the discharge a pixel needs time to become active again. This time can be characterize with the so-called "**recovery time**" with a time constant given by

$$\tau = \mathrm{R_Q} \cdot \mathrm{C_D} \ , \tag{3.1}$$

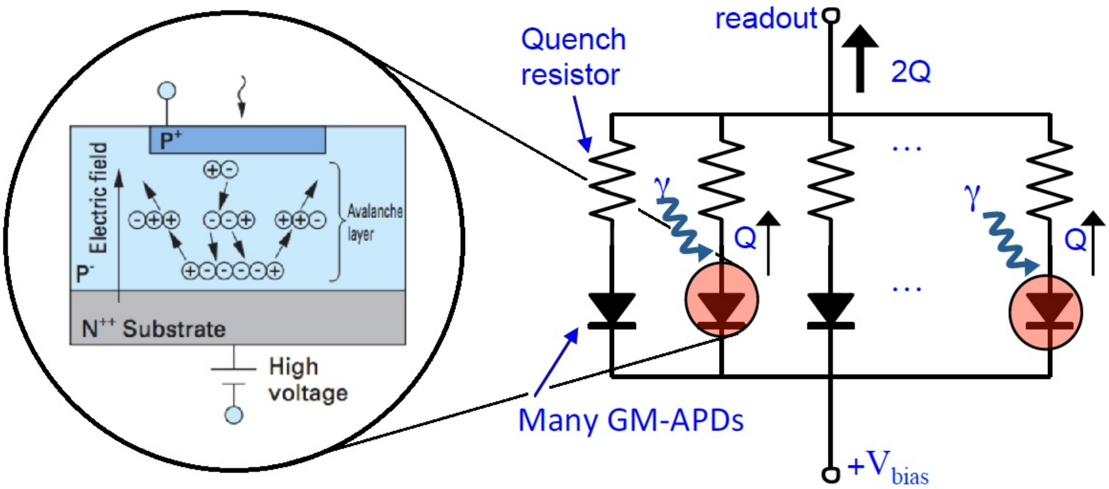

Figure 3.2: Schematic figure of the APDs arranged in an array with individual quench resistors shows the working principle of an SiPM. The figure is based on [10].

where $\mathrm{C_D}$ is the capacitance of the avalanche volume inside the APD. Usually the recovery time is around 10-30 ns [11].

In the case of an ideal photodetector, the output signal is linearly proportional to the entire range of the input light intensity. However, in a real detector the linearity is limited. The smallest detectable signal is determined by the noise, while the upper detection is limit is given by the saturation due to the limited number of pixels. From these properties follows that the SiPM is fundamentally a non-linear device. The response function of an SiPM can be approximated with the following empirical formula [12]

$$\mathrm{R} \propto \mathrm{N_{f.p.}} = \mathrm{N_{total}} \cdot (1 - \mathrm{e}^{-\frac{\mathrm{N_{p.e.}} \cdot \mathrm{PDE}}{\mathrm{N_{total}}}}) \ , \tag{3.2}$$

where R is the amplitude of the electrical output, $\mathrm{N_{f.p.}}$ is the number of fired pixels, $\mathrm{N_{total}}$ is the total number of pixels in the diode and $\mathrm{N_{p.e.}}$ is the number of photons in a pulse. The PDE is the **photon detection efficiency**. The applicability of this formula requires light distribution over the pixels and short light pulses compared to the pixel recovery time [13].

The PDE can be divided into three main components [10]

$$\mathrm{PDE}(\lambda, \mathrm{U}, \mathrm{T}) = \mathrm{QE}(\lambda) \cdot \epsilon_{\mathrm{aval}} \cdot \mathrm{GE} \ , \tag{3.3}$$

where $\mathrm{QE}(\lambda)$ is the wavelength-dependent quantum efficiency for photons to create a primary photoelectron, ϵ_{aval} is the probability to create an avalanche and GE is a geometrical fill factor which quantifies the ratio of the active area compared to the

total area of the detector. The typical photon detection efficiency of an SiPM is around 30 % for blue light [10].
The intrinsic amplification of an SiPM called **gain** (G) is defined as the number of electric charges generated by one Geiger discharge in an SiPM pixel [10]

$$G = \frac{1}{e} \cdot Q_{\text{Geiger discharge}} \ . \tag{3.4}$$

The typical gain values are in the range of $10^5 - 10^6$.
For the operations of SiPMs, thermal noise, afterpulses and crosstalk play an important role.
An electron can make a transition from the valence band to the conduction band after an interaction with the vibrating crystal lattice (thermal charge carrier generation) or even spontaneously (tunneling). A thermal/tunneling charge carrier generation can trigger an avalanche, even if no photons or other particle passed the APD. This phenomena is called **thermal noise** whose signal is similar to a pulse created by photoelectrons. The amount of noise-pulses increases with temperature and can reach a few MHz [10].
The silicon lattice of the APDs contains impurities where the ionization charges can be trapped for a certain time and get released leading to a delayed appearance of the avalanche. The delay-time can vary, usually up to several hundred nanoseconds. It follows that the pulse from such a delayed avalanche will initiate after the "normal" pulse. In this case, the read out signal is distorted or includes additional pulses [10]. This phenomenon is called **afterpulse** (see in Figure 3.3).
A fired pixel can initiate an avalanche also in its neighboring cells if photons have enough energy to create an electron-hole pair in a neighboring pixel. In that case the detected charge is similar to a pulse corresponding to two or more photoelectrons. The rate of this **optical crosstalk** can be reduced with the separation of neighboring pixels, for example by inserting so-called trenches between the pixels. The rate of crosstalk also decreases with increasing pixel size since the emitted photon can be reabsorbed with higher probability in the same pixel [11]. According to the technical data sheet of the SiPM under study [14], the crosstalk probability is around 1 %. A schematic drawing explaining optical crosstalk is given in Figure 3.3.

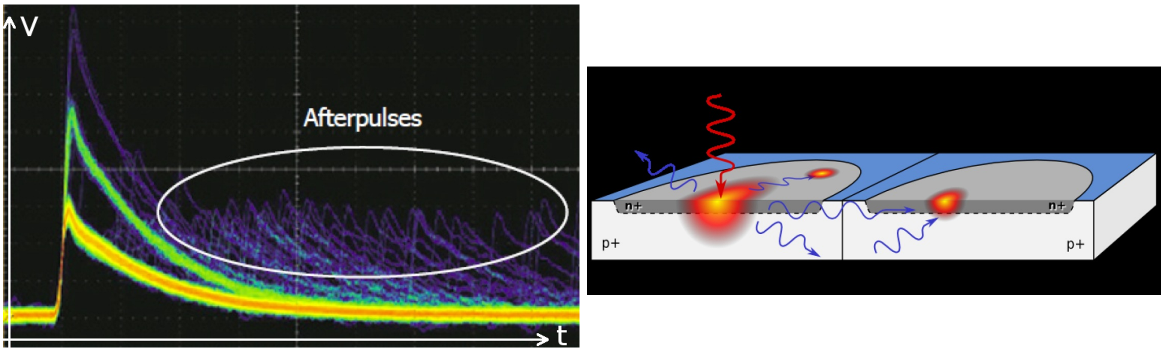

Figure 3.3: Right panel: The read out signal of an SiPM is shown for long measurement time. The pulse can be disorted or includes additional afterpulses caused by an untrapped ionization charge. The figure is based on [13]. Left panel: Scenario for interpixel crosstalk shown for two neighboring pixels [15].

3.2 The working principle of a scintillator

When charged particles traverse a scintillator, a fraction of the energy can be deposited in its material by exciting the medium along the trajectory. Molecules of the substances emit a few percentage of this energy as optical photons, called scintillation [16]. The emitted light can be detected by photo-sensitive detectors such as Photo Multiplier Tubes (PMT) or SiPMs coupled to the scintillator. Wavelength shifting fibers and optical grease are sometimes used together with a scintillator, the first one in case the detection wavelength range of the photo detector does not match with the wavelength emitted by the scintillator. In our case, the scintillator produces light with frequency well matched to the SiPM and good contact and stable reproducibility of the measurement are ensured without the use of optical grease. Therefore neither wavelength shifting fibers nor the optical grease are needed in our setup.
The tiles used in this study are EJ-200 plastic scintillators [17], with sizes of $10 \times 10 \times 2\,\text{mm}^3$, $15 \times 15 \times 2\,\text{mm}^3$ and $20 \times 20 \times 2\,\text{mm}^3$. In order to increase the measured light yield, the tile is surrounded by reflective materials, such as 3M foil [18] or reflective paint [19]. Since the SiPM is directly coupled to the side of the scintillator tile, in the preparation of the coating, a small, approximately ($2 \times 2\,\text{mm}^2$) window is left open for the SiPM.

3.3 The electron gun setup

In Figure 3.4, a schematic illustration of the experimental setup for the scintillator tile investigations read out by an SiPM is shown. In Figure 3.5 the close environment

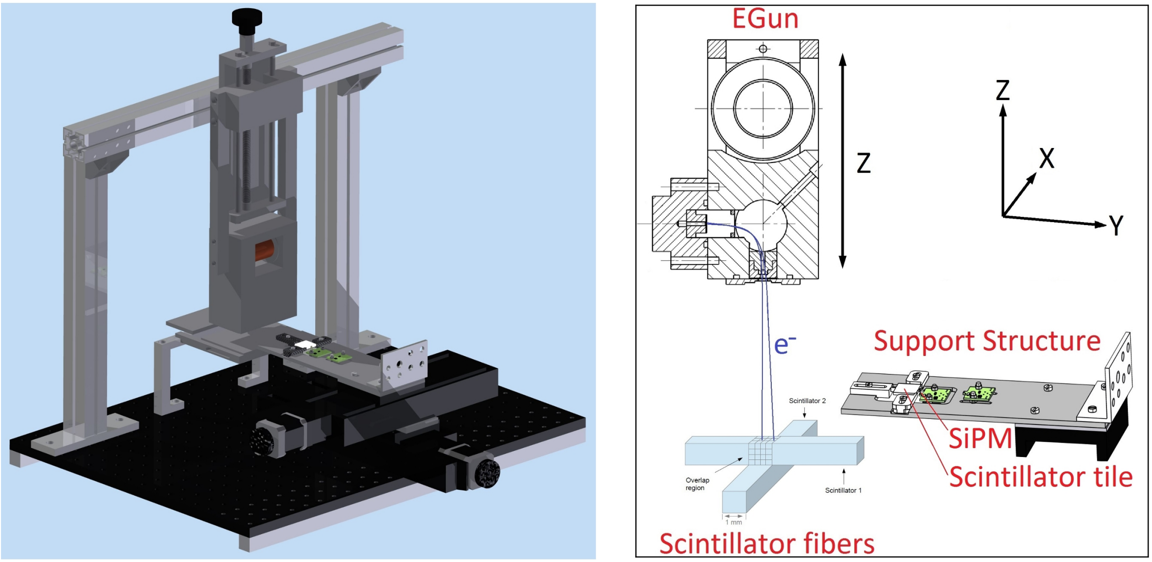

Figure 3.4: Left panel: An illustration of the scintillator tile scan setup. Right panel: A schematic of the setup showing its main parts. Figure is based on [20].

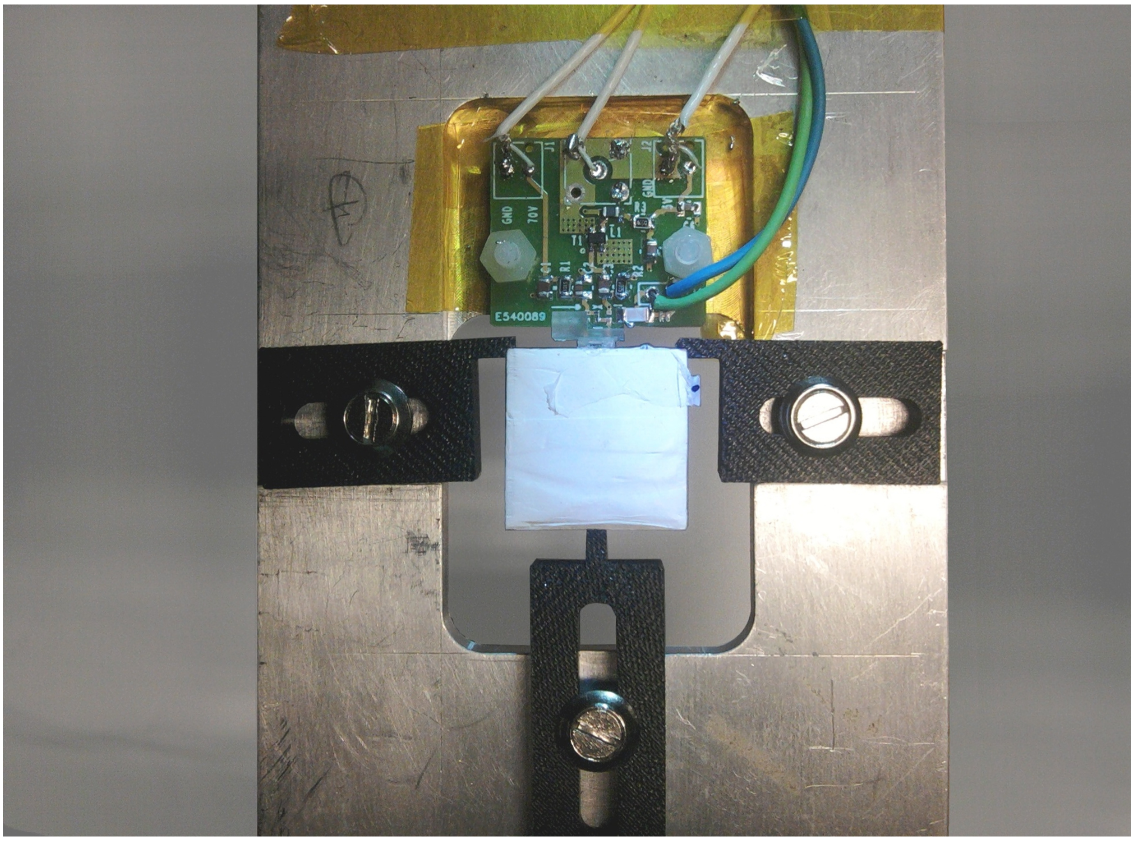

Figure 3.5: The scintillator tile with the PCB, the SiPM and the tile holders.

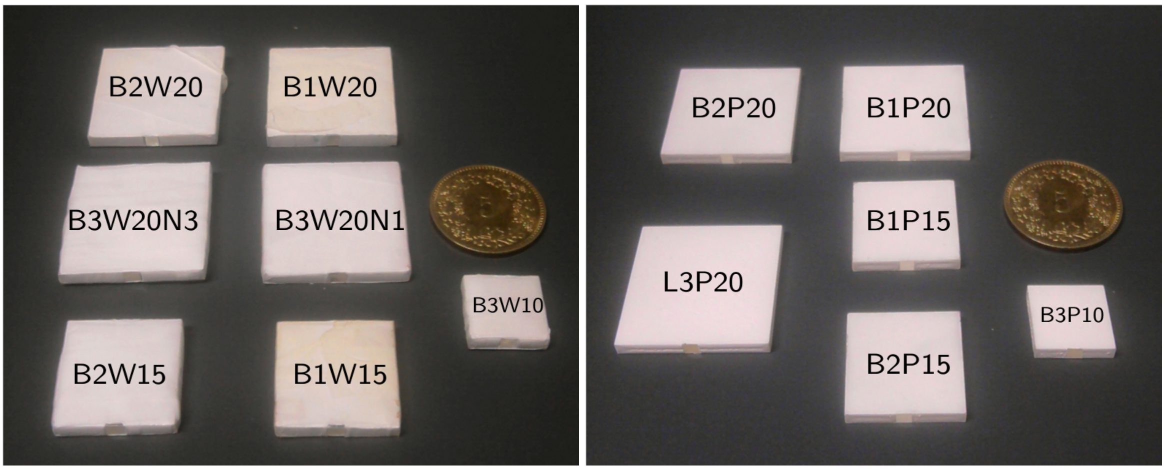

Figure 3.6: The scintillator tile set includes three sizes and two coatings. The width of all scintillator tiles is 2 mm. Left panel: The tiles are surrounded by 3M reflective foil. Right panel: The tiles are covered by reflective paint.

of the scintillator tile is shown. The setup is used for characterization of the tiles with different sizes and coatings. This includes the investigation of the signal uniformity within the tile and the edge-effects, the determination of the average light yield for the scintillator tiles with different features and the light crosstalk at the common edge for multitile arrangements. The setup is installed in a darkroom. To control the temperature inside the dark room a fan, an air conditioner and two radiators are used. The data acquisition system as well as the power supplies are situated in a neighboring room connected via a light-tight cable feed-through.

The experimental setup can be divided into the following main parts:

1. **The Electron Gun:** To obtain ionizing radiation for the studies on the scintillator tiles, a β^- emitting, approximately 350 MBq ^{90}Sr isotope is used [21]. The source in combination with the decay of the daughter nucleus ^{90}Y provides a continuous electron energy spectrum up to approximately 2 MeV. The β^- decay products of the decay chain are the following:

$$^{90}\mathrm{Sr} \longmapsto {}^{90}\mathrm{Y}(\longmapsto {}^{90}\mathrm{Zr} + \mathrm{e}_2^- + \overline{\nu_e}) + \mathrm{e}_1^- + \overline{\nu_e} \tag{3.5}$$

   The source is installed in a solid tungsten container and thus well shielded. To know the deposited energy of the traversing electrons in the scintillator material, Minimum Ionizing Particles (MIP) can be selected by an electron monochromator. The MIPs are charged particles with mean energy loss rate

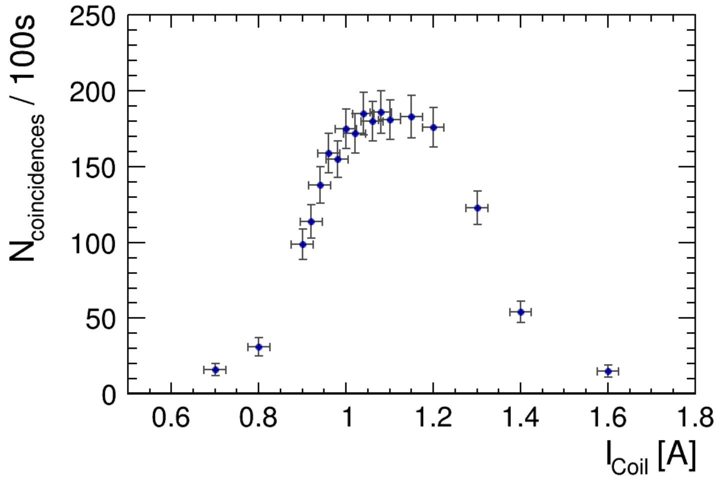

Figure 3.7: The number of coincidences per 100 s as a function of the current of the coil in the monochromator. During the measurement a scintillator tile was placed between the electron gun and the trigger fibers.

close to the minimum [16]. The ionization loss of MIPs only slightly depends on their momentum. Changing the magnetic field created by a coil the MIP electrons from the energy spectrum of the radioactive source can be selected. Electrons above 1 MeV can be considered to be MIPs, and can traverse the scintillator tiles under study (thickness 2 mm) [21]. To decrease the covered area of the beam on the tile, thereby to increase the position resolution of a tile scan, the electron beam is collimated using collimators right after the source and at the exit of the tungsten body.

2. **The Trigger fibers:** Below the electron gun and the scintillator tile two scintillator fibers are installed orthogonally to each other. The vertical distance from the exit of the electron gun is 27 mm. The shape of one fiber is a cuboid with $1 \times 1\,\mathrm{mm}^2$ square basic, thereby the overlap region of the fibers in the e^- beam direction is also $1\,\mathrm{mm}^2$. The fibers are read out each with an SiPM. The signals of the SiPMs are transferred to a Nuclear Instrumentation Module (NIM) to select the signals in coincidence. The output of this unit is used to trigger the data acquisition of the main SiPM coupled to the scintillator tile.
In order to achieve the highest data taking rate the maximal amount of the traversing electrons per time unit should be selected by adjusting the current of the electron monochromator. To find the corresponding current a scintillator tile from our collection (see in Section 8.1.2) was placed between the electron

gun and the trigger fibers and the number of coincidences was measured as a function of the current of the monochromator coil. As shown in Figure 3.7, the maximum data taking rate in the setup is reached when using approximately $I_{coil} = 1.05\,A$.

3. **The movable table:** In the interest of scanning the whole area of a scintillator with appropriate accuracy, it needs to be moved with sub-millimeter precision with respect to the electron beam position. The precise movement ($< \pm 0.03\,mm$) of the platform which hosts the scintillator tile and the SiPM including the amplification board and read out is ensured by two independently operable LTM 80M-170 stepper motors [22] orthogonally to each other in the horizontal plane. The motors can be operated automatically controlled by the read out interface.

4. **Printed Circuit Board:** The Printed Circuit Board (PCB) is soldered directly to the contacts of the SiPM and amplifies its signal with a BGA614 broadband matched amplifier [23]. The voltage regulator which supplies the BGA614 preamplifier is supplied with a voltage of 5.5 V in order to gain an amplification factor weakly dependent on the input voltage. One PCB represents an amplification stage with approximately a factor of 9. The PCB also host a PT1000 thermometer close to the SiPM in order to monitor the temperature during the data taking. The SiPM is biased by an external high voltage supply with a constant voltage a few Volts above the breakdown voltage. In the case of the Hamamatsu MPPC S13360-1325PE a bias voltage of 57.8 V is recommended by the vendor for a temperature of 25 °C.

5. **Powering and controls:** The signal of the SiPM is recorded by a digital oscilloscope named PicoScope 6404B with sampling rate of 5 GS/s [24]. The PicoScope and the stepper motors are connected to a personal computer and controlled by a customized LabView program [25] used as the read out interface. The low voltage for the pre-amplifiers is provided by a Gossen 33K7 power supply, for the bias voltage of the SiPM a Keithley 2410 power supply is used and the current for the coil of the electron monochromator is provided by a SM7929-D power supply. A FLUKE 45 multimeter is connected in parallel to the low voltage supply to monitor the input voltage.

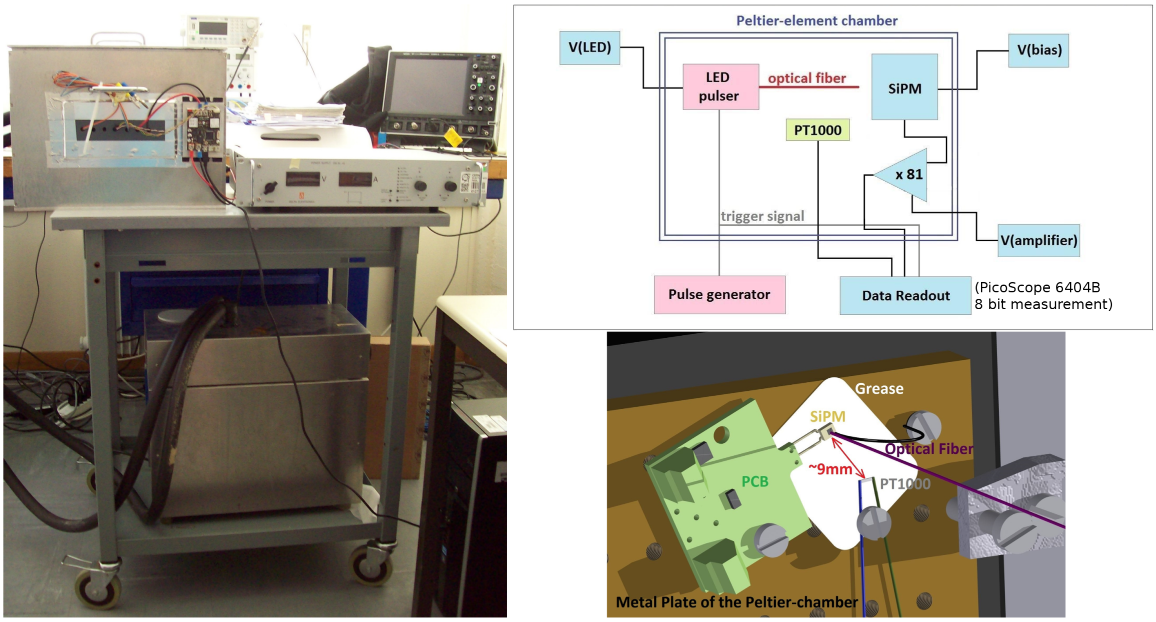

Figure 3.8: Left panel: Thermally isolated Peltier-element chamber is shown together with its supplementary equipments. Right, top panel: A schematic of the experimental setup illustrates the measurement for the gain of the SiPM. Right, bottom panel: The SiPM and its surrounding in the interior of the temperature controlled chamber.

3.4 The LED pulser setup

Figure 3.8 shows the setup equipped with a light emitting diode (LED) including a thermally isolated Peltier-element chamber with a temperature range covering the region of interest (15 °C - 30 °C) together with its auxiliary equipment. The schematic of the experimental setup illustrates the working principle of the measurement for the intrinsic amplification of the SiPM as a function of the temperature and of the overvoltage. In addition an illustration of the SiPM and its surrounding in the interior of the temperature controlled chamber is shown. Instead of a scintillator tile, a LED connected to a pulse generator is directed onto the active surface of the SiPM by an optical fiber. The interior of the Peltier-element chamber is shielded against light. The power supplies and the read out of the SiPM and of the PCB are the same as in the scintillator tile scan setup described in Section 3.3. However, for triggering the input signal of the LED pulser is used, which is a square pulse which is usually operated with a peak to peak voltage of 4 V and with a frequency of 10 kHz. Both the voltage and the frequency can be modified.

The SiPM is placed close to the metal plate of the Peltier-element chamber whose

temperature is adjustable with an absolute accuracy of ±0.2 °C. The temperature of the SiPMs vicinity is monitored both by a thermometer of the Peltier-element chamber itself located on the metal plate and by a PT1000 thermometer placed close to the SiPM with same accuracy like the thermometer of the Peltier-element chamber. Between all these components thermally conductive grease is used to ensure a good heat flow. The two temperatures are in agreement within the uncertainty of the temperature sensors.
The PCB connected to the SiPM, its input voltage, the high voltage for biasing the SiPM and the other parts of the experimental setup except the scintillator tile are operating as discussed in Section 3.3. The voltage used for biasing the SiPM and the pre-amplifier voltage of the PCB are the same as in the scintillator tile scan pulser setup. The main differences are the number of the PCBs and the coupling of the SiPM. In order to cope with the lower output signal of the SiPM due to the decreased number of photons in comparison to the tile scan setup, two amplifiers are used in series resulting to an amplification factor of 81. The PCB of the LED pulser contains two inputs. Through the PIN connector, the power supply for the LED is ensured. Changing the supply voltage, one can control the intensity of the emitted light. The LEMO connector is connected to the output of a PicoScope used as pulse generator for the trigger signal for the LED. The same signal is used to trigger the LED pulser and to read out the SiPM signal.

Chapter 4

Data reconstruction

In the following chapter, the steps of data processing will be introduced, including the data acquisition with the PicoScope, the online data management with a user interface based on a customized LabView program and the offline data analysis.

4.1 The electron gun signal

4.1.1 The user interface of the customized LabView program

The PicoScope which processes the data of the SiPM under test as well as the trigger signal is connected to a computer. The data from its output is processed by a customized LabView program of which user interface is shown in Figure 4.1. The program provides the possibility to monitor and record the SiPMs signal in real time. It also records the data taking parameter such as the temperature measured with a PT1000 thermometer, the measurement date and time provided by a PC, the number of coincidences counted by the LabView program itself, the positions of the scintillator tile with respect to the electron gun read out from the electronic module of the stepper motors. The bias voltage which supplies the SiPM, and the current of the coil in the electron monochromator are given manually to the program before the program run. With the user interface the dynamic ranges of the Channel A and B read outs can be adjusted. The dynamic range should be chosen neither to cut the pulse nor lose precision. Since the amplitude of the SiPM pulse varies in a wide range the upper limit of the dynamic range of Channel A was always chosen to be at least twice the average pulse height to avoid cutting into the SiPM pulse. In most of the cases 500 mV was sufficient. In Channel B the trigger threshold should not exceed the amplitude of the square pulse signal of the NIM logic which is slightly below 1 V.

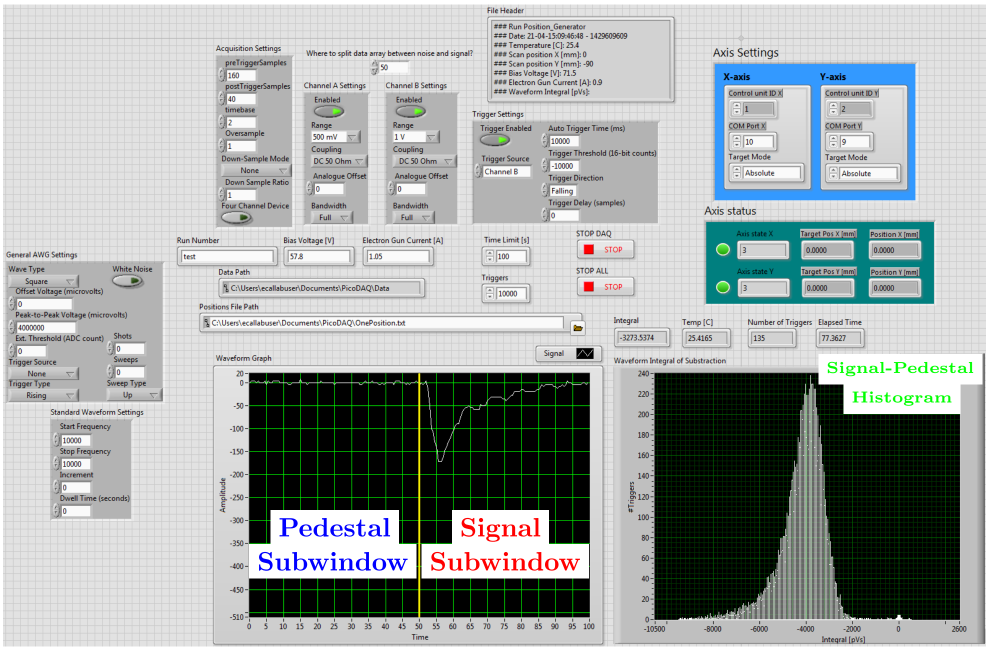

Figure 4.1: The user interface of the LabView program. Beside the data taking parameters, the SiPM response is displayed on a graph for each triggered event. This graph is divided into two subwindows for the pedestal and for the signal of the electron traverses through the scintillator tile. On the histogram (right, below) the result of the subtraction of the integrals of both subwindows is displayed for all event that we recorded during one data taking.

The output current of the SiPM coupled to the scintillator tile is amplified by the pre-amplifier board and multiplied by the coupling resistance of the PicoScope. This modified output signal is shown as a function of the time on the oscilloscope-like display of the user interface on the left side. Taking advantage of the continuous data buffering of the PicoScope, the beginning of the SiPM's pulse, can be shifted to the middle of the measurement window. Thereby, the entire measurement window can be divided into two subwindows with equal length of time (see in Figure 4.1). The first subwindow called Pedestal-subwindow records the signal height in the absence of a signal. The second one called Signal-subwindow records the signal pulse just after the trigger on top of the current pedestal value. The LabView program integrates online the signal and the pedestal response separately in their time subwindows to make a conversion to charge and subtracts the pedestal from the signal integral. Like that, the signal is corrected for shifts in the pedestal height, which was observed in previous studies. The integral of the Pedestal-subwindow, the Signal-subwindow and the Signal-Pedestal-subwindow (s-p. subwindow) are saved for offline data analysis.

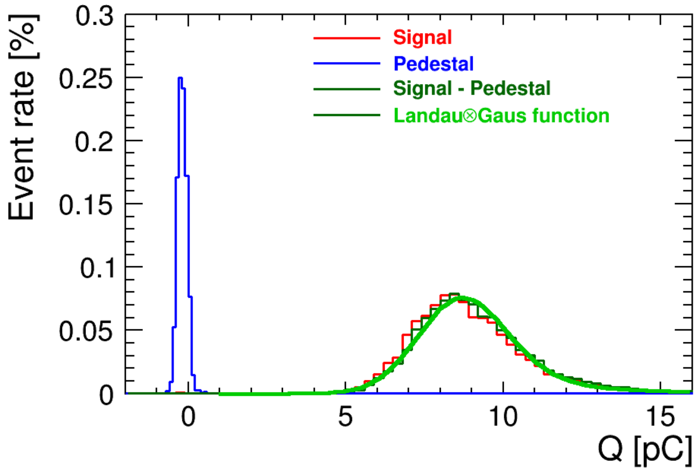

Figure 4.2: Charge distributions of the pedestal, the signal and the signal-pedestal. One can observe that the mean of the pedestal distribution has a shift from the zero charge. The signal-pedestal distribution is fitted by a Landau Gaussian convolution.

4.1.2 The offline data analysis

The output file of the LabView program is analyzed by the ROOT object-oriented program based on the C++ programming language [26]. The integrated charge for all APDs in the SiPM can be calculated by dividing the integral values in the signal-pedestal subwindow by the coupling resistance of the PicoScope (50 Ω) and by the amplification factor of the BGA amplifier (factor 9)

$$\mathrm{Q_{SiPM}} = \frac{\int_{\text{s-p. subwindow size}} \mathrm{V}_{\text{s-p. subwindow}}(t)\,\mathrm{d}t}{\mathrm{R_{coupling}} \cdot \text{amplification}} \ . \tag{4.1}$$

The resulting charge distribution for an example measurement is displayed in Figure 4.2. The distribution of the deposited energy caused by the fluctuations in the ionization of a charged particle in a thin layer of material follows a Landau-distribution [27].

The measured distribution also contains a component of statistical fluctuations due to the intrinsic accuracy of the measurement. Therefore the signal distribution is best described by a convolution of a Landau distribution and a Gaussian distribution [28]. The function has four free parameters: the Landau-scale factor which quantifies the shape of the distribution which varies between 0 and 1; the most probable value (MPV); the total area (A) and the width of the Gaussian function (σ). In the following, the MPV as well as the arithmetic mean of the distribution are used in the comparison of the SiPM response for different measurement conditions and tile features. The mean of the distribution can easily be calculated, therefore providing a stable and fast result independent of the fit quality. The use of the MPV together with the other parameters of the fit can give global information about the SiPM response, but the fit is time-consuming and can lead to unstable results in case of a low number of events.

4.2 The LED pulser signal

Since the LabView program is the same in the case of both setups, the data acquisition for the LED measurement is similar to the one of the electron gun signal. The only difference is realized in the charge distribution of the signal-pedestal subwindow. Since the APDs within the SiPM operates in Geiger mode, the output is quantized by the unit of the Geiger discharge of a cell, caused by one photo-electron. It follows that the charge spectrum consists of single photo-electron peaks as shown in Figure 4.3, of which number is in correlation with the emitted amount of light of the pulser. The photo-electron peaks can be broadened by thermal noise, crosstalk, afterpulses and by the unevenness between the response of individual APDs. These effects increase with increasing number of the photo-electrons. The height of the different peaks follows a Poisson distribution. These effects limit the maximum number of separable peaks from the background in the charge spectrum. In addition, the light intensity of the LED can be changed. If the LED intensity is low, fewer peaks occur in the photo-electron spectrum. On the other hand, a large LED light intensity results in more noise (Section 5.1.2.5).
In order to obtain the distance between the neighboring photo-electron peaks, which equals the gain of the SiPM multiplied by the elementary charge as written in Equation 3.4, the electron spectrum is fitted. For the fit,1 separate Gaussian functions are used which individual amplitudes follow a Poisson distribution.

$$\mathrm{f_i}(\mathrm{q}, \mathrm{A_{Poiss}}, \mathrm{n_{peak}}, \lambda, \mathrm{Q_{noise}}, \mathrm{d}, \sigma_\mathrm{i}) = \mathrm{A_{Poiss}} \cdot \mathbf{Poisson}(\mathrm{n_{peak}}; \lambda) \cdot \mathbf{Gauss}(\mathrm{q}; \mathrm{Q_{noise}} + \mathrm{i} \cdot \mathrm{d}; \sigma_\mathrm{i}) \ . \tag{4.2}$$

In the function, the global parameters are the amplitude of the Poisson distribution ($\mathrm{A_{Poiss}}$), the expected average number of photo-electrons in the Poisson distribution (λ), the position of the pedestal peak ($\mathrm{Q_{noise}}$), the distance between all photo-electron peaks (d), and the number of the fitted peaks ($\mathrm{n_{peak}}$). $\mathrm{n_{peak}}$ is optimized by an algorithm which checks whether the broadening of the last peak does not exceed a cut-off value that is derived from the width of the third photo-electron peak. $\sigma_{\mathrm{PE}i}$ is the

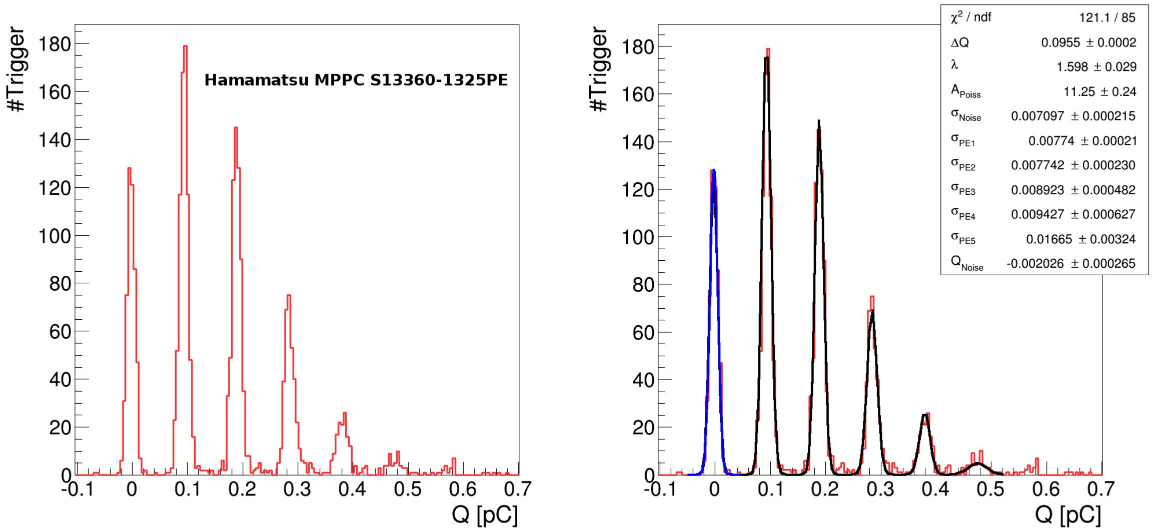

Figure 4.3: Left panel: The charge spectrum of an SiPM contains single photo-electron peaks. The number of visible peaks correlate with the emitted light yield of the LED pulser. Right panel: A fit of the photo-electron spectrum with Equation 4.2. One can observe the increasing width of the photo-electron peaks with increasing ordinal number.

width of the i^{th} Gaussian fit where i means the number of the photo-electron peak and runs from 1 to n_{peak}. The width of the noise peak is parametrized by σ_{Noise}. The finally obtained variables are the results of an iterative fitting procedure in order to increase the stability of the fit function with many parameters.
A typical photo-electron spectrum and the result of a fit with Equation 4.2 is shown in Figure 4.3. The first peak is the pedestal peak, marked with blue color, located around at 0 pC. The subsequent peaks, marked in black color, are the photo-electron peaks. All peaks are separated by the same distance. The more photons are measured, the broader is the peak, shown by the increase in the width from σ_{PE1} to σ_{PE5}. This is due to the increased impact of noise, crosstalk, afterpulses and slightly different response between individual pixels.

It should be noted that the study of different SiPMs was done, however, it would go beyond the scope of this thesis to discuss the analysis of these data, too.

Chapter 5

Systematic uncertainties

This chapter presents the most relevant systematic uncertainties, which can occur in both experimental setups as well as during the data evaluation processes.

5.1 The LED pulser data

In this section the systematic uncertainties related to the LED pulser setup and the subsequent data analysis will be studied. These include influences on the following effects: the histogram bin width, the number of fitted peaks, the measurement duration, the reproducibility, the dynamic range and the LED pulser settings.

5.1.1 Uncertainties of the photo-electron fit

5.1.1.1 Histogram bin width

The photo-electron spectrum is saved in a histogram with a fixed bin width. The number of the bins is adjusted to the investigated features of the data and that the features in the data distribution can be resolved with. The number of bins is varied in order to observe the effect on the extracted SiPM gain. The study was repeated for different data sets with similar results. The left panel of Figure 5.1 shows the extracted gain as a function of the number of bins between two neighboring photo-electron peaks. The gain values are in agreement within the uncertainties for 10 to 50 bins between two adjacent photo-electron peaks and the dispersion of the gain value is negligibly small. Therefore, the width of the bins does not influence the gain within that range. It is worth noting that the uncertainty on the fitted gain decreases slowly with the number of bins, while the corresponding computing time increases rapidly. As a compromise, for further studies 20 bins between the neighboring peaks are used.

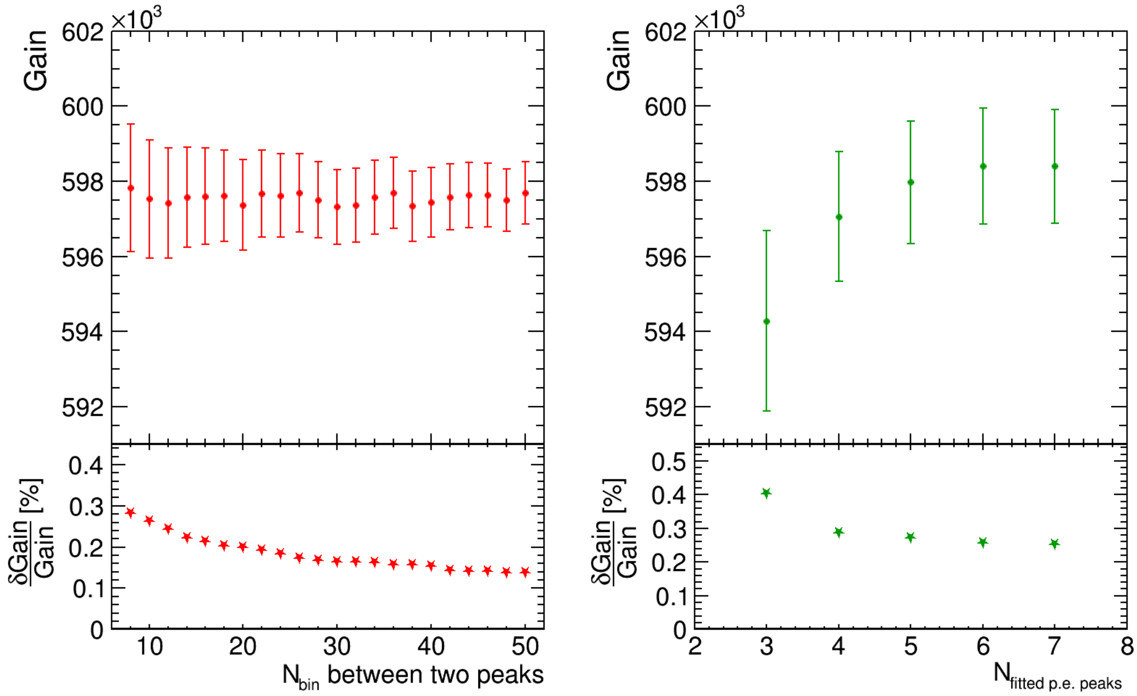

Figure 5.1: Left panel: The gain versus the number of bins between two neighboring peaks. In the range of 10 to 50 bins between two adjacent peaks, the dependence is significantly smaller than the measurement accuracy. Right panel: The gain as a function of the number of fitted photo-electron peaks. In the range of 5-7 fitted photo-electron peaks there is no significant dependence on the choice of the number.

5.1.1.2 Number of fitted photo-electron peaks

The impact of the number of the fitted photo-electron peaks on the extracted gain for a fixed LED amplitude is shown in the right panel of Figure 5.1. Theoretically, all neighboring photo-electron peaks should be equidistant from each other since with an SiPM the multiple of the APD charge can be measured. Nonetheless, Figure 5.1 shows that the gain increases as a function of the number of fitted peaks. At $N_{peak} = 6$ the extracted gain saturates. In the data analysis, between 5 and 7 peaks are used for estimating the gain. In this range, taking into account the uncertainty of the gain, the results do not differ. Similarly to the number of bins, the uncertainty of the fitted gain also decreases with increasing number of fitted peaks. Therefore a maximum number of photo-electron peaks is chosen that can be distinguished from the background (see Section 4.2).

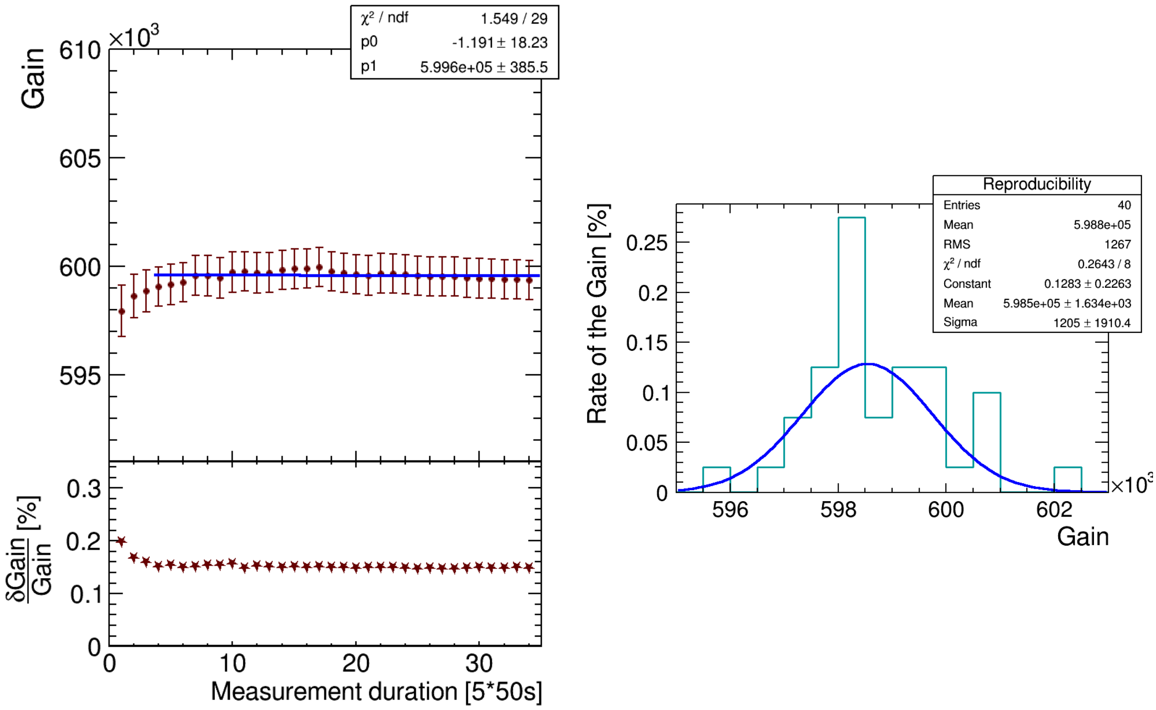

Figure 5.2: Left panel: The estimated gain as a function of the measurement duration. After the initial period, the gain and its uncertainty stabilize. Right panel: The gain is measured several times for $5 \cdot 50\,\text{s}$ using the same experimental conditions. The gain evolution is fitted with a Gaussian function. The gain values have a spread of 0.2% using the sigma/mean ratio of the fitted Gauss.

5.1.2 Uncertainties of the experimental setup

5.1.2.1 Measurement duration

The length of the measurement duration is a compromise between reaching a large number of events collected during the measurement and the effective use of the resources. In order to identify an appropriate measurement duration and to investigate its systematic uncertainty, the gain was measured for data sets with increasing measurement times. The results are plotted in the left panel of Figure 5.2. The data sets are recorded in units of 50 s. This is due to the fact that the temperature is recorded at the start of all measurements. After $4 \times 50\,\text{s}$ measurements duration, the gain values and the uncertainties are stable. Additional measurement time does not change the gain value and its uncertainty. For future studies $5 \times 50\,\text{s}$ long measurements are used.

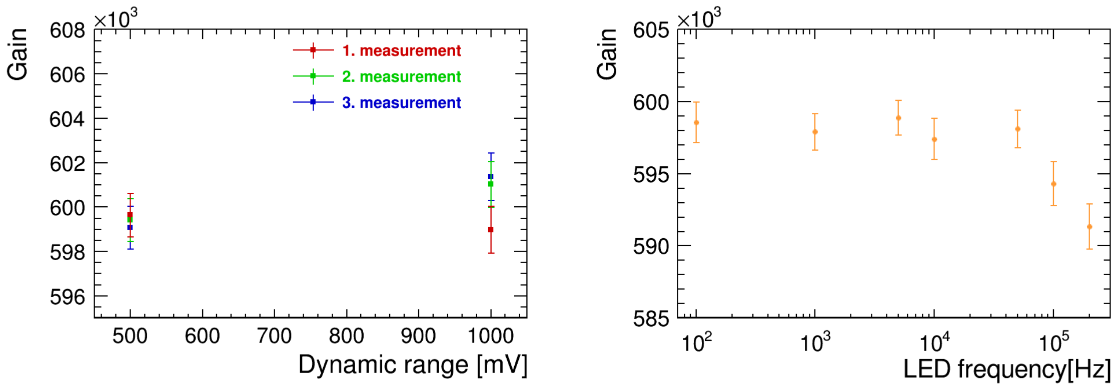

Figure 5.3: Left panel: The estimated gain is measured three times for two dynamic ranges. The values with same dynamic range agree, the average gain obtained with 500 mV and 1000 mV differ by up to 0.5%. Right panel: The estimated gain as a function of the LED pulser's frequency. Up to 50 kHz the gain values are in agreement with each other within the uncertainties.

5.1.2.2 Reproducibility

As a cross check on the stability of the measurement under the same experimental conditions, the estimated gain was studied for several data sets (right panel of Figure 5.2). The gain values fill a histogram and the uncertainty of the reproducibility is determined as the standard deviation of the distribution. Since the relative uncertainty (the standard deviation divided by the mean) is approximate 0.2%, the gain measurements are considered reproducible within this uncertainty.

5.1.2.3 Dynamic range

To cope with the different output signal of the SiPM for various setups, the dynamic range of the input channel of the PicoScope can be adjusted. With the change of the dynamic range, a small shift of the baseline in the oscilloscope was observed. In order to investigate the possible impact of this effect on the measurement results, the gain was measured three times for a fixed LED amplitude with dynamic range values of 500 mV and 1000 mV. The results are displayed in the left panel of Figure 5.3. As shown in the reproducibility study (see in Section 5.1.2.2), the data sets with the same dynamic range agree within the uncertainties. However, the mean of the three measurements for the two different dynamic ranges differ by up to 0.5%.

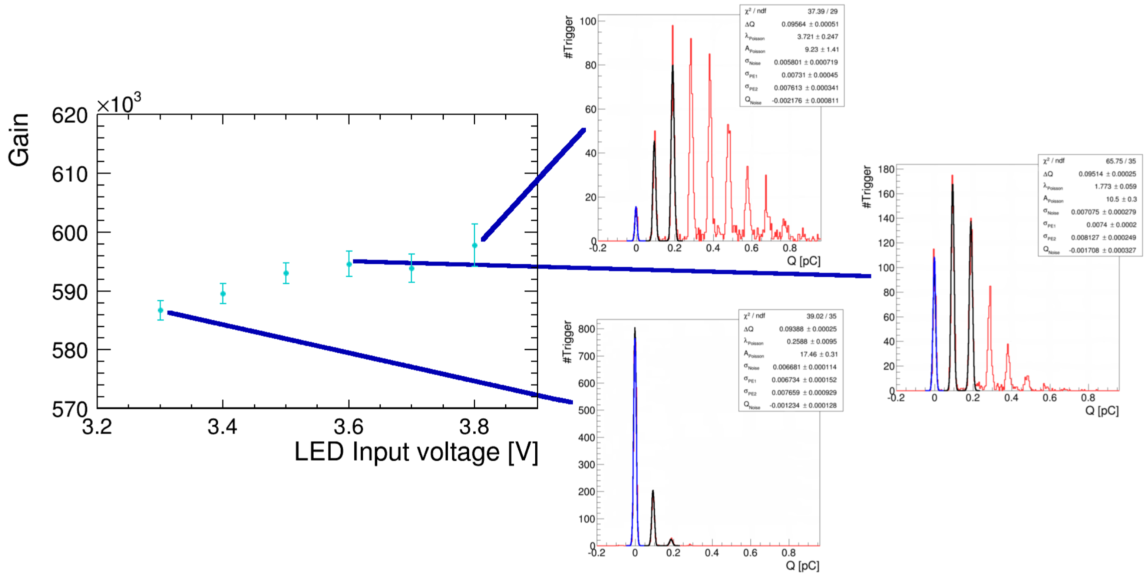

Figure 5.4: The gain as the function of voltage of a LED pulser. With increasing LED intensity the gain increases. The charge spectra are fitted always with 3 peaks to avoid other systematic effects.

5.1.2.4 The input frequency of the LED pulser

In order to combine high measurement speed with stable results, the LED frequency rate should be well selected. The maximum available frequency is limited by the construction of the LED pulser. The estimated gain was studied as a function of the input frequency of the LED pulser (LED frequency). As shown in the right panel of Figure 5.3, the gain starts to decrease above 50 kHz. To avoid a shift in the measured gain of the SiPM depending on the chosen frequency, the frequency of the PicoScope output channel is set always to 10 kHz.

5.1.2.5 LED light yield

In Figure 5.4, the estimated gain is studied as a function of the LED intensity which increases with increasing LED input voltage. It should be noted that the light yield also depends on other hardly-controllable settings such as the angle of the optical fiber compared to the surface of the SiPM and the distance between the end of the fiber and the SiPM cells. Accordingly, the optical fiber is directed orthogonally to the SiPM's surface and the distance between these components is kept constant at a few mm. It should be also noted that the SiPM is fundamentally a non-linear device. Due to the finite number of pixels, the response signal for the incoming photons saturates

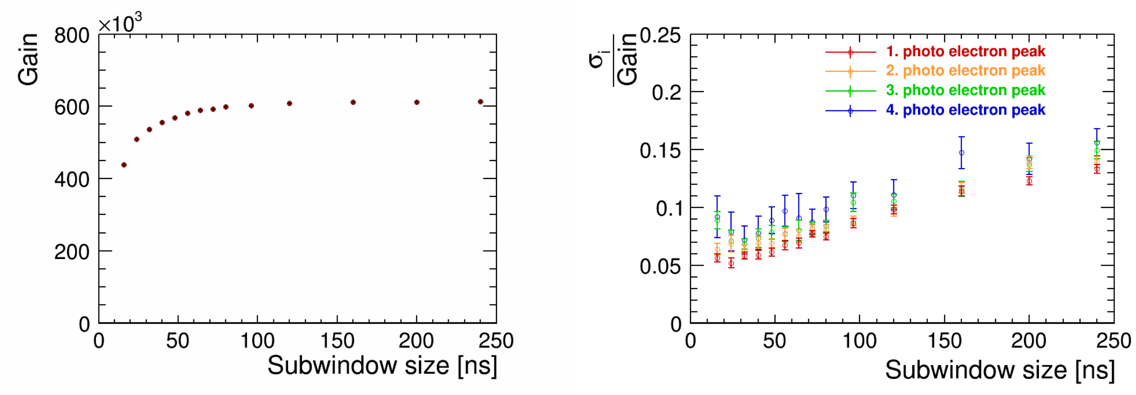

Figure 5.5: Left panel: The estimated gain as a function of the events time window size. Right panel: The resolution of the first four photo-electron peaks as a function of the events time window size.

at the scale of the total number of pixels. However, number of photons reaching the SiPM is far below from this level both, in the LED pulser setup and in the scintillator tile scan setup cases.

To quantify the uncertainty coming from the variation of the number of photons reaching the active area of the SiPM, the gain is studied as a function of the input voltage of the LED pulser. In order not to bias the result by the number of fitted photo-electron peaks, only the first three peaks of the charge spectrum are fitted independent of the available peak number. Figure 5.4 shows the obtained results and some example charge distributions. The estimated gain increases as a function of the emitted light yield.In the case of measurements with the above mentioned optical fiber alignment, the input voltage of the LED changes in the range of 3.5 V - 3.7 V. Within that range the signal spectrum comprises at least 6 photo-electron peaks, as shown in Figure 5.4 if $(\text{Input Voltage})_{\text{LED}}$ is within this range. The uncertainty of the estimated gain is calculated for 3.5 V - 3.7 V, which corresponds to systematic uncertainties of $\pm$ 0.35%.

5.1.2.6 Events time window size

The measured gain of the SiPM is studied as a function of the length on the time window, as explained in Section 4.1.1. The gain increases with increasing time window (see Figure 5.5 left), while the photo-electron peak broadens (see Figure 5.5 right). As a result, the resolution of the peaks deteriorates for large time window sizes. A window size of 80 ns is chosen as a compromise between gain stability and peak width.

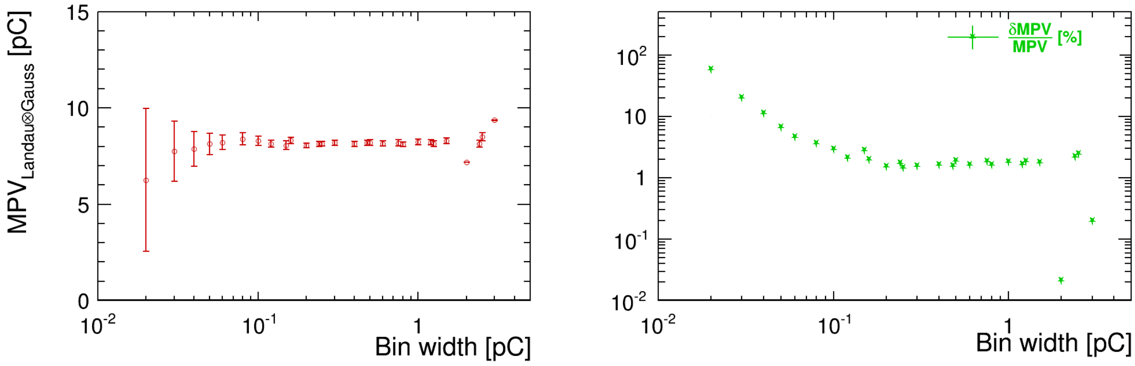

Figure 5.6: Left panel: The MPV of the Landau Gauss convolution is plotted as a function of the histogram bin size. Right panel: The uncertainty of the MPV of the Landau Gauss convolution as a function of the histogram bin size.

5.2 The electron gun data

In this section the systematic uncertainties of the tile scan setup and the subsequent data analysis are presented. These include the histogram bin width, the measurement time, the reproducibility and the uncertainty caused by the temperature correction.

5.2.1 Histogram bin width

Similar to the evaluation of the SiPM gain, the charge spectrum of the scintillator tile setup is saved in a histogram with fixed bin width. When fitting the distribution with a Landau-Gauss convolution, as explained in section 4.1.2, the fit results may depend on the chosen bin width. The results are shown in Figure 5.6. While the mean of the distribution remains essentially independent of the bin width, it is important to check the most probable value (MPV) of the signal and its uncertainty as a function of the bin width. For better visibility, the x-axis has a logarithmic scale. Between a bin width of $0.15 - 1$ pC the MPV values are stable and agree within the measurement accuracy. The uncertainty δMPV/MPV reaches a minimum of approximately 2% for a bin width of 0.2 pC which is used in the following.

5.2.2 Reproducibility

In order to quantify the reproducibility of the measurement, charge distributions measured under the same experimental conditions are compared to each other. For the characterization of the distribution, the mean value of the charge distribution and the most probable value of the Landau Gauss convolution are determined for each

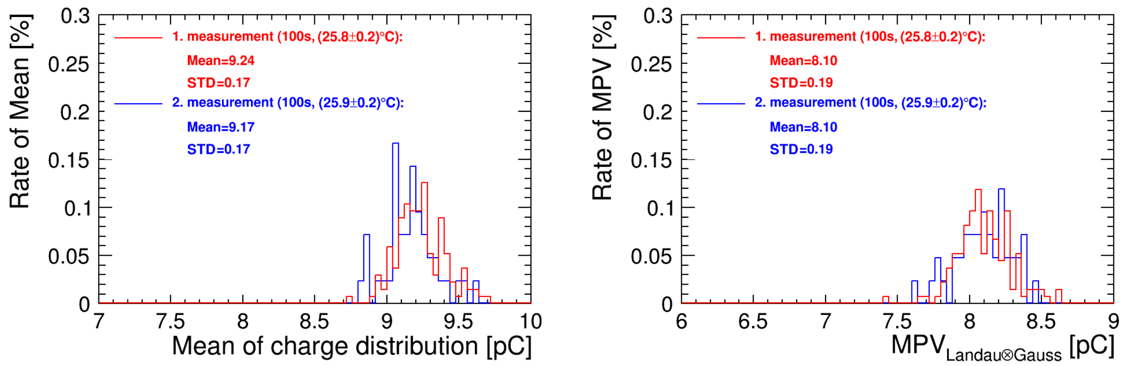

Figure 5.7: Left panel: The distribution of the mean of the charge spectrum for 100 s long measurements. Right panel: The distribution of the MPV of the Landau Gauss convolution for 100 s long measurements. In both cases the standard deviation of the distribution is approximately 2%.

measurement. The MPV and mean values of repeated measurements are entered in a histogram shown in Figure 5.7. The standard deviation of the distribution is an indication of the reproducibility of the measurement. The obtained uncertainty for 100 s long measurements is approximately 2% in both cases.

5.2.3 Measurement time

The process described in Section 5.2.2 is repeated for datasets with increased measurement time. Figure 5.8 shows the standard deviation over mean values for both the Mean and the MPV of the signal distributions as a function of the measurement time for otherwise identical experimental conditions. The measurement time is expressed in the number of coincident triggers at a rate of $1.5-2$ triggers/s. The standard deviation values are expected to depend linearly on the inverse of the square-root of the number of triggers. This is indeed the case, as can be seen from Figure 5.8. The fitted linear function is taken into consideration according to the systematic uncertainty of the measurement time.

5.2.4 Events time window size

Similarly to Section 5.1.2.6, the length of the measurement window for an event can be adjusted. In the left panel of Figure 4.1.1 the mean of the charge distribution and the MPV of the Landau Gaussian convolution is studied as a function of the size of the event time window. As in the LED pulser setup, the SiPM response has

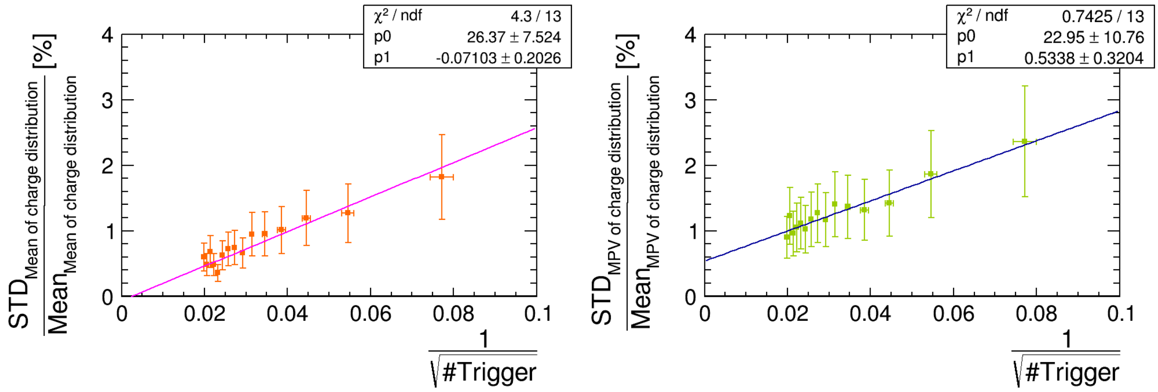

Figure 5.8: Left panel: the standard deviation (STD) divided by the mean values are calculated from the mean of the charge distribution and studied as a function of the inverse square root of the number of triggers. The dataset is fitted by a linear function. Right panel: The same quantities are plotted for the MPV of the charge distribution and also fitted by a linear function.

a dependence on the length of the event time window. However, contrary to the trend line of the gain (Figure 5.2), the mean and the MPV values have a maximum at around 80 ns. To obtain a comparable result between both setups, the events time window size is also set to 80 ns.

5.2.5 Temperature correction

In order to avoid the unwanted bias in the measured charge during for instance a tile scan, the datasets are corrected to a reference temperature. The temperature correction method is described in detail in Section 7.1. The temperature correction takes the following form

$$\mathrm{Q}^{\mathrm{corrected}}(\mathrm{T}) = \frac{1}{1 + \alpha_{\mathrm{r}} \cdot (\mathrm{T} - \mathrm{T}_{\mathrm{ref}})} \cdot \mathrm{Q}^{\mathrm{measured}}(\mathrm{T}) \tag{5.1}$$

where α_{r} represents a relative correction factor for temperature. This parameter can be obtained from the temperature calibration of the SiPM (see Section 7.1). In an ideal case, the measurements with same experimental conditions but with different temperatures agree after the temperature correction.

Here, the mean of charge values and the MPV values after the temperature correction are fitted with a linear function. The temperature dependency is studied by the slope of the first order polynomial. The result is shown in the right panel of Figure 5.9. The slopes for both fitted functions are zero within uncertainty. However, both datasets

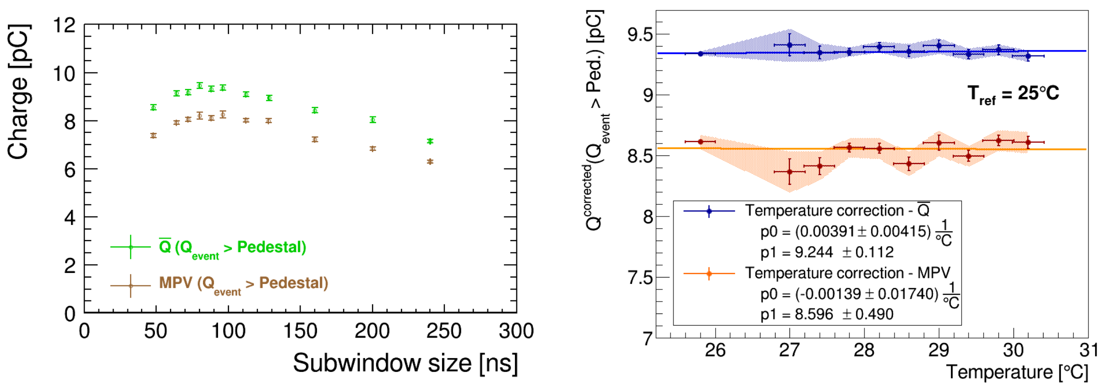

Figure 5.9: Left panel: The mean of the charge distributions and the MPV of the Landau Gauss convolutions as a function of the events time window size. Right panel: Investigation of the temperature correction in the case of the mean and the MPV of the charge distribution.

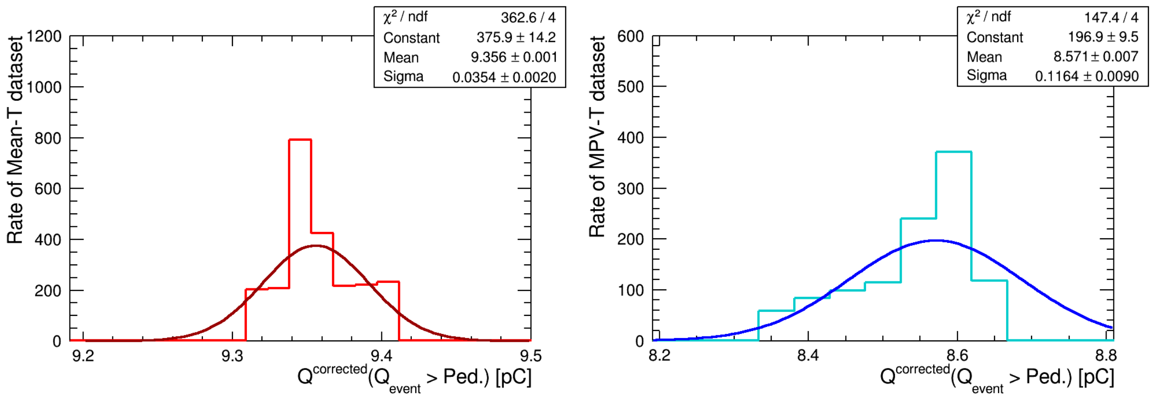

Figure 5.10: Left panel: The spread of the data using the mean of the charge distributions after temperature correction fitted by a Gaussian function. Right panel: The spread of the data using the MPV of the charge distributions after temperature correction fitted by a Gaussian function.

have a fluctuation around the intersection of the constant functions (p1) which equals the charge at the reference temperature. The spreads of the dataset for the mean of the charge and for the MPV of the charge are shown in Figure 5.10. It is also worth noting that both intersections of the linear fits (p1) are in agreement with the $Q^{corrected}$ values within uncertainties with the corrected values in Section 7.1.

Chapter 6

Overvoltage calibration

The breakdown voltage of an avalanche photodiode (V_{bd}) is the minimum reverse bias voltage (V_{bias}) which allows the self-sustaining avalanche multiplication in the SiPM. To obtain an SiPM gain larger than zero, the SiPM should be supplied with a bias voltage higher than the breakdown voltage. By definition, the difference between the bias voltage and the breakdown voltage is the overvoltage (V_{over})

$$V_{over} = |V_{bias} - V_{bd}| \ . \tag{6.1}$$

By increasing of the overvoltage, the gain of the SiPM can be increased. The noise also increases with the overvoltage. Taking these two competing effects into account, an optimal operation voltage for each individual SiPM can be identified. The optimal value is usually suggested by the vendor. The gain (G) of the SiPM depends linearly on the overvoltage for a range of few volts above the breakdown voltage [10]

$$G = \frac{C_D}{e} \cdot (V_{bias} - V_{bd}) = \frac{C_D}{e} \cdot V_{over} \ . \tag{6.2}$$

Here, C_D is the capacitance of the avalanche volume inside an APD and e represents the elementary charge.
In order to determine the breakdown voltage of the SiPM under study, the gain of the SiPM was measured for different bias voltage values above the breakdown voltage. The measurement was taken with the LED pulser setup (Section 3.4), while the temperature was controlled and set to a constant value of 25 °C throughout the measurement. The measured gain for various bias Voltages V_{bias} was fitted to a linear function. As a result, the breakdown voltage can be calculated from the fit parameters. The breakdown voltage is the voltage at which the gain would be zero. The results are shown in Figure 6.1.
For the use of the SiPM (Hamamatsu MPPC S13360-1325PE), the vendor suggested

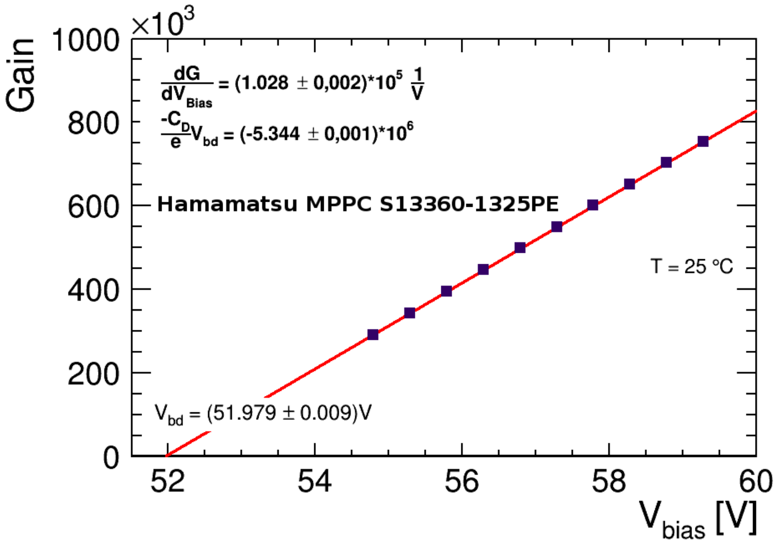

Figure 6.1: The gain is studied as a function of the bias voltage. From the linear fit, the breakdown voltage and the capacitance of the APDs can be determined.

an optimal bias voltage 57.80 V. This corresponds to an overvoltage of (5.82 ± 0.03) V, while the gain is $(51.98 \pm 0.01) \cdot 10^5$. In the following studies $V_{\text{bias}} = (57.80 \pm 0.05)$ V is used for all measurements.

Chapter 7

Temperature correction of the SiPM response

With increasing temperature, thermal vibrations in the silicon lattice of the SiPM increase. This leads to a decreased free path length of electrons in the avalanche and a reduction of the electron avalanche. Hence, the gain as well as the breakdown voltage of an SiPM depend on the temperature: the gain decreases and the breakdown voltage increases with increasing temperature. In order to ensure an SiPM signal independent of the temperature, it is necessary to regulate or measure the temperature during data taking at a fixed bias voltage. In the following, the temperature dependence of the SiPM response is studied once in terms of the charge recorded in tile scans and once in terms of the SiPM gain. The bias voltage and the temperature of the SiPM under study are controlled within $\pm 0.025\,\mathrm{V}$ and $\pm 0.2\,^{\circ}\mathrm{C}$) and the bias voltage is fixed to $57.8\,\mathrm{V}$ which corresponds to an overvoltage of $(5.82 \pm 0.03)\,\mathrm{V}$ at $25\,^{\circ}\mathrm{C}$. The evaluation of the temperature dependence is facilitated due to the fact that the SiPM is operated within a temperature range, in which the temperature dependence of the SiPM response is expected to follow a linear dependence.

7.1 Charge dependency on the temperature

In the following, the SiPM response is studied via the charge recorded in a tile scan as introduced in Chapter 3.3 and Equation 4.1. In the dark room, in which the tile scan setup is located, the temperature can be modified with an air conditioning (A.C.), a fan and radiators. In addition changes of the outside temperature due to the weather influence the SiPM temperature. In the vicinity of the silicon sensor heat sources exist, such as the preamplifier on the PCB and the coil of the electron monochromator. To obtain a stable SiPM temperature despite these heat sources,

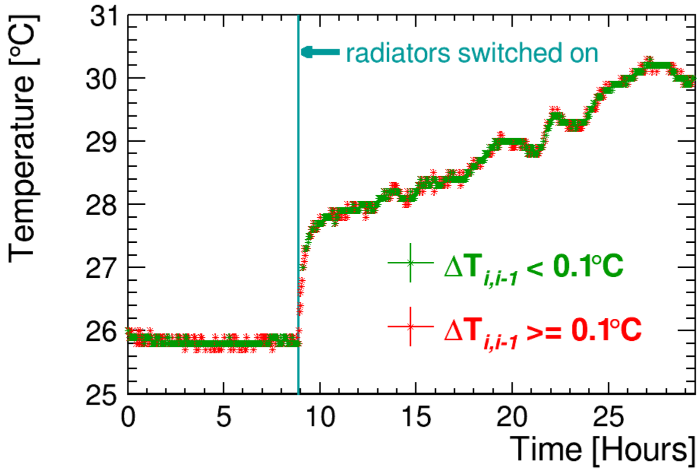

Figure 7.1: The dataset of the charge versus temperature calibration. Data points with $\Delta T_{i,i-1} >= 0.1\,°C$ are rejected from further analysis steps and marked with red stars.

a fan is directed onto the setup. The temperature of the SiPM is monitored with a PT1000 thermometer close to the sensor with $(0.150 + |T| \cdot 0.002)\,°C$ accuracy [29], where T is the temperature in °C.
The SiPM is coupled to a scintillator tile which is in the following a with 3M foil wrapped tile with $20 \times 20 \times 2\,mm^3$ size. The scintillator tile is placed such that the electron beam traverses the middle of the tile. Data are recorded in 100 s long measurements. In order to widen the measured temperature range, after half of the measurement time the radiators are turned on. As shown in Figure 7.1, the radiators are switched on 9 hours after the start of the data taking. After additional 15 hours, the influence of the radiators reaches a maximum after which the SiPM temperature change is related to the changes of the weather. Subsequent dataset of 100 s measurement time are rejected if the temperature of the previous dataset differs by at least ±0.1°C. All remaining data files of the same temperature are combined to one data set. The mean values of the SiPM response per temperature are evaluated in two different ways as introduced in Section 4.1.2:

1. The mean value of the charge distribution,
2. The MPV of a Landau-Gauss fit of the charge distribution.

The SiPM response in terms of charge as a function of the temperature is shown in Figure 7.2 for the two methods. As discussed for Section 4.1.2, the MPV has

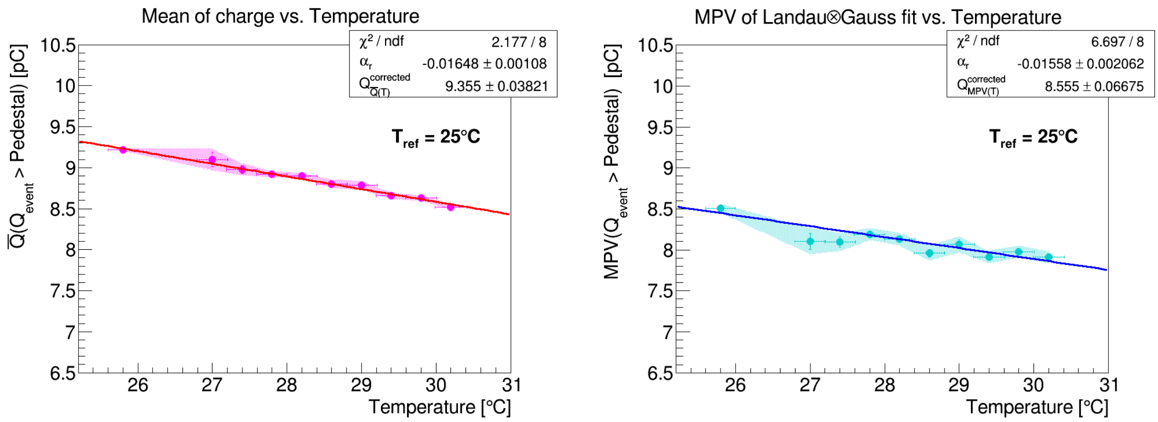

Figure 7.2: Left panel: The charge versus temperature using the mean of the charge distribution. Right panel: The MPV of the Landau Gauss convolution fit versus temperature. The shaded areas indicate the combination of statistical and systematic uncertainties.

systematically lower numbers than the mean value due to the tail of the charge distribution towards large Q values.

The temperature dependence can be described by

$$Q^{\text{corrected}} = \frac{1}{1 + \alpha_r \cdot (T - T_{\text{ref}})} \cdot Q^{\text{measured}}(T), \tag{7.1}$$

used for the temperature correction of the SiPM responses [30]. The function can be transformed into a linear representation,

$$Q^{\text{measured}}(T) = \alpha_r \cdot Q^{\text{corrected}} \cdot T + Q^{\text{corrected}} \cdot (1 - \alpha_r \cdot T_{\text{ref}}). \tag{7.2}$$

The first parameter of the linear fit is the relative temperature coefficient $\alpha_r \left[\frac{\%}{°C}\right]$. It shows by how many percent the charge varies for a 1 °C temperature change. Using Equation 7.2, α_r is given by

$$\alpha_r = \frac{dQ^{\text{measured}}(T)}{dT} \cdot \frac{1}{Q^{\text{measured}}(T_{\text{ref}})} \,. \tag{7.3}$$

The second parameter of the linear fit is the charge value after temperature correction $Q^{\text{corrected}}$. The relative temperature coefficients for the $\overline{Q}$ and MPV measurement extrated from Figure 7.2 are in agreement with each other, $\alpha_{r;\overline{Q}(T)}^{\text{S13360-1325PE}} / \alpha_{r;\text{MPV}(T)}^{\text{S13360-1325PE}} = (95 \pm 13)\%$. The mean of charge measurement gives a more stable result. Therefore, in the following the results of the mean of the charge distribution are used in the temperature calibration. For a Hamamatsu MPPC S13360-1325PE and a wrapped scintillator tile with $20 \times 20 \times 2\text{mm}^3$ size, the relative temperature coefficient is

$$\alpha_{r;\overline{Q}(T)}^{\text{S13360-1325PE}} = (-1.648 \pm 0.056)\,\frac{\%}{°C}. \tag{7.4}$$

The charge of the SiPM response changes by 1.648 % for a 1 °C change in the temperature.

7.2 Gain dependency on the temperature

In the following the SiPM response is studied via the SiPM gain. The gain dependency on the temperature was studied using the LED pulser setup (Chapter 3.3) and Equation 4.1. The setup is placed in a thermally isolated Peltier-element chamber. The SiPM temperature is regulated by a thermally controlled metal plate and good heat flow between the plate and the SiPM is ensured by using thermally conductive grease between all components. The tested temperature range is from 15.5°C to 29.5°C and scanned twice, in opposite directions in steps of 2°C, starting with the highest temperature, going to the lowest temperature ("down" measurement) and again back to the highest temperature ("up" measurement). Between each steps 4 minutes are used to achieve a thermal stabilization of all components. The SiPM response to the LED pulser is recorded for 10 times 50 s. The temperature variation during this $10 \cdot 50$ s period is within the uncertainty of the temperature sensors.
During the measurement the temperature is monitored with a PT1000 thermometer close to the SiPM and with a temperature sensor integrated in the Peltier-element itself. The values measured with these thermometers are in agreement within 0% to 2%. However, the differences between the two temperature measurements change with temperature (see in the left panel of Figure 7.3). For the temperature calibration of the SiPM, the temperature of the PT1000 is used and the uncertainty is extracted from the technical data sheet.

The gain is extracted from the photo-electron spectra as introduced in Section 4.2. Then the gain vs. temperature distribution for both (up, down) measurements are fitted with a similar linear function like in Equation 7.2,

$$G^{measured}(T) = \beta_r \cdot G^{corrected} \cdot T + G^{corrected} \cdot (1 - \beta_r \cdot T_{ref}) \ . \tag{7.5}$$

The parameters of the two fits agree within the uncertainties, the datasets with the same temperature are combined. The fit of the combined measurement (see in Figure 7.3) contains a relative temperature coefficient parameter (β_r) and a $G^{corrected}$ parameter, which are similar to those presented in Equation 7.2

$$\beta_r = \frac{dG(T)}{dT} \cdot \frac{1}{G(T_{ref})}. \tag{7.6}$$

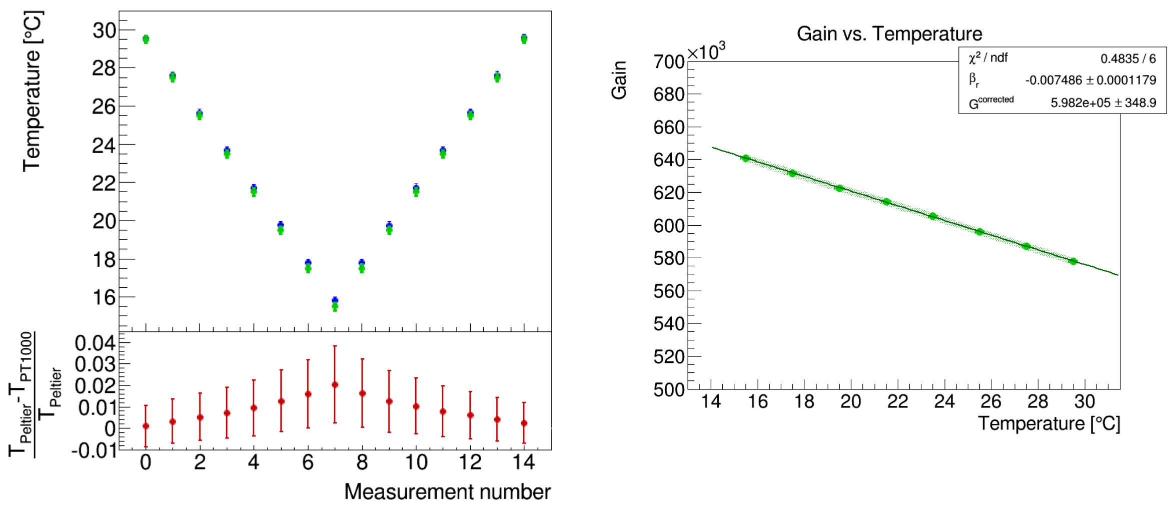

Figure 7.3: Left panel: The temperatures measured with the PT1000 thermometer and with the thermometer of the Peltier-element. The two temperature measurements are in agreement within 0% to 2%, the differences change with temperature. Right panel: The SiPM gain as a function of the temperature. The dependency is calculated as a combination of the gain measurements scanned in opposite directions in temperature. The shaded areas indicate the combination of statistical and systematic uncertainties.

Based on the measurements of the SiPM under study the temperature coefficient related to the gain has a value of

$$\beta_r^{\text{S13360-1325PE}} = (-0.749 \pm 0.003)\,\frac{\%}{^\circ\text{C}}\ . \tag{7.7}$$

Therefore the gain of the SiPM response changes with 0.75 % for a 1 °C change in the temperature.

7.3 Relation between gain and charge dependence

The difference between the temperature coefficient obtained from the charge versus temperature $\alpha_{r;\overline{Q}(T)}^{\text{S13360-1325PE}} = (-1.648 \pm 0.056)\,\frac{\%}{^\circ\text{C}}$ and the gain versus temperature calibrations $\beta_r^{\text{S13360-1325PE}} = (-0,749 \pm 0.003)\,\frac{\%}{^\circ\text{C}}$ is explained in the following. As can be seen from the uncertainties the conditions for temperature control are much better in the Peltier-element chamber $\left(\frac{\delta(\alpha_r^{\text{S13360-1325PE}})}{\alpha_r^{\text{S13360-1325PE}}} \approx 10 \cdot \frac{\delta(\beta_r^{\text{S13360-1325PE}})}{\beta_r^{\text{S13360-1325PE}}}\right)$, but it is too small to host the tile scan setup. In this section an attempt will be made to define the relation in analytic way between the above-mentioned coefficients and to outline a possible explanation for the difference. Then, theoretically derived values will be compared to the measured ones.

As it was shown in Equations 7.3 and 7.6, the temperature coefficients of the charge (α_r) and of the gain (β_r) are by definition:

$$\alpha_r = \frac{dQ(T)}{dT} \cdot \frac{1}{Q(T_{ref})}$$
$$\beta_r = \frac{dG(T)}{dT} \cdot \frac{1}{G(T_{ref})}$$

According to [12], the response of the SiPM can be written as

$$R \propto N_{f.p.} = N_{total} \cdot (1 - e^{-\frac{N_{p.e.} \cdot PDE}{N_{total}}}) \,, \tag{7.8}$$

where R is the amplitude of the electrical output, $N_{f.p.}$ is the number of fired pixels, N_{total} is the total number of pixels in the diode and $N_{p.e.}$ is the number of photons in a pulse. The PDE is the photon detection efficiency, which depends on the overvoltage ($V_{over}(T)$)[14]. In the case of the scintillator tile scan setup the number of the fired pixels is in order of hundred, using the LED pulser setup the number of fired pixels are less with a factor of 10. The total number of pixels is 2668, the PDE is less than 30%. Thus, the exponent in Equation 7.8 is much below one, Equation 7.8 can be approximated with its 1. order Taylor-polynomial around 0,

$$R \propto N_{p.e.} \cdot PDE(\lambda; V_{over}(T)). \tag{7.9}$$

It is assumed that the charge of the SiPM response (Q) measured with a scope is proportional to the amplitude of the electrical output of the SiPM

$$Q \propto R \,, \tag{7.10}$$

where the charge of the SiPM response can be given by

$$Q(T) = A \cdot B(V_{over}(T)) \cdot G(T) \;. \tag{7.11}$$

Here A is a proportionality factor

$$A \propto e \cdot N_{p.e.} \,, \tag{7.12}$$

which contains only the temperature independent quantities like the elementary charge (e) and the number of photons in a pulse ($N_{p.e.}$).

$B(V_{over}(T))$ contains all factors which depend on the overvoltage thus also on the temperature

$$B(V_{over}(T)) \propto PDE(\lambda; V_{over}(T)) = QE(\lambda) \cdot \varepsilon(V_{over}(T)) \cdot GE \ . \tag{7.13}$$

In this case, the photon detection efficiency (PDE) is a known component in B which depends on the overvoltage [10]. QE is the quantum efficiency, GE is a geometrical fill factor and $\varepsilon(V_{over}(T))$ is the probability to develop an avalanche in an APD.
Based on these equations and approximations, the temperature coefficients of the charge (α_r) can be calculated. For simplification, $B(V_{over}(T))$ will be written as B in the equations. First, the derivative of charge of the SiPM response can be written as

$$\begin{aligned} \frac{dQ(T)}{dT} &= A \cdot B \cdot \frac{dG(T)}{dT} + A \cdot \frac{dB}{dT} \cdot G(T) = \\ &= A \cdot B \cdot \frac{dG(T)}{dT} + A \cdot \frac{dB}{dV_{over}} \cdot \frac{dV_{over}}{dT} \cdot G(T) \ . \end{aligned} \tag{7.14}$$

The expanded member of the derivative can be written using Equation 6.2

$$V_{over}(T) = \frac{e}{C_D} \cdot G(T) \qquad \Big/ \frac{d}{dT} \tag{7.15}$$

$$\frac{dV_{over}(T)}{dT} = \frac{e}{C_D} \cdot \frac{dG(T)}{dT} \ , \tag{7.16}$$

thereby

$$\frac{dQ(T)}{dT} = A \cdot B \cdot \frac{dG(T)}{dT} + A \cdot \frac{dB}{dV_{over}} \cdot \frac{e}{C_D} \frac{dG(T)}{dT} \cdot G(T) \ . \tag{7.17}$$

The exact form of the overvoltage dependency of B is not known. In the following B is approximated with two models.

7.3.1 "Linear charge" model

The model described in the following should be considered only as an instructive example. Here it is assumed that the temperature dependence of B can be neglected

$$\frac{dB}{dT} = 0 \ , \tag{7.18}$$

the PDE as a function of the overvoltage is approximated with a constant function shown in the left panel of Figure 7.4. With this assumption, in Equation 7.14 can be modified to

$$\frac{dQ(T)}{dT} = A \cdot B \cdot \frac{dG(T)}{dT} + 0 \ . \tag{7.19}$$

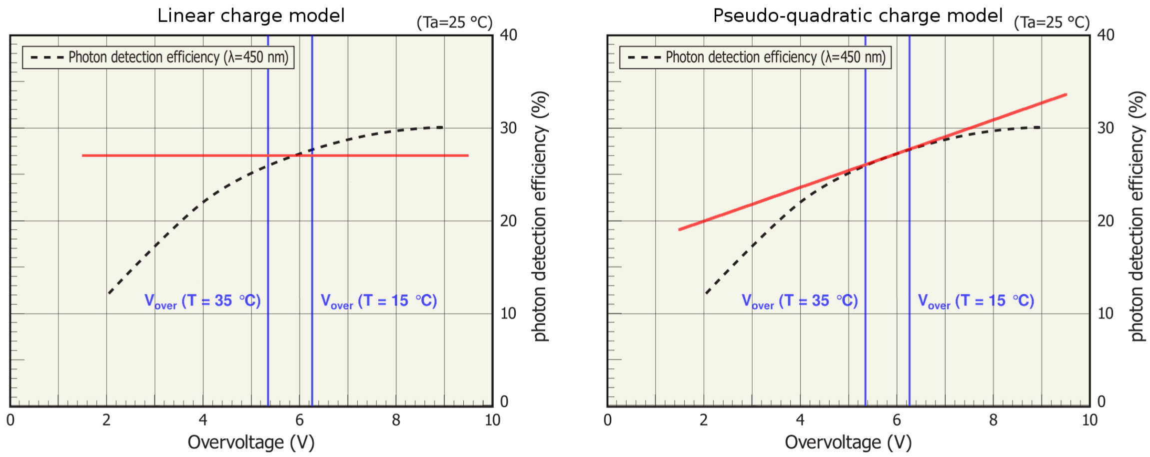

Figure 7.4: The photon detection efficiency as a function of the overvoltage. The borders of the overvoltage variation caused by the temperature fluctuations are marked with blue lines. Between these lines the mentioned dependency is fitted with a constant function (neither overvoltage and nor temperature dependency) in the case of the "linear charge model" (left panel) and with a linear function in the case of the "pseudo-quadratic charge model" (right panel). Both figures are based on [14].

The charge of the SiPM response at the reference temperature is then given by

$$Q(T_{ref}) = A \cdot B \cdot G(T_{ref}) \ . \tag{7.20}$$

Using Equation 7.19 and 7.20, the relative temperature coefficients of charge and gain are identical

$$\alpha_r = \frac{dQ}{dT} \cdot \frac{1}{Q(T_{ref})} = \frac{dG(T)}{dT} \cdot \frac{1}{G(T_{ref})} = \beta_r \ . \tag{7.21}$$

Hence, the temperature coefficients of the charge and of the gain are the same, if the charge of the SiPM response has only the gain as a temperature dependent parameter. Indirectly, since the temperature coefficient of the gain and the charge are not equal, the charge of the SiPM response should contain at least one more parameter which is temperature dependent in addition to the gain.

7.3.2 "Pseudo-quadratic charge" model

In the previous section it was found that, if there is no temperature dependent parameter in the charge of the SiPM response except for the gain, the temperature coefficient of the gain and the charge are identical. Since this result does not agree with the measurements as a next step it is assumed that the SiPM charge has a linear dependency on the overvoltage, given by

$$\mathrm{B} = \mathrm{a} \cdot \mathrm{V_{over}(T)} + \mathrm{b} = \mathrm{a} \cdot \frac{e}{\mathrm{C_D}} \mathrm{G(T)} + \mathrm{b} \tag{7.22}$$

and

$$\frac{\mathrm{dB}}{\mathrm{dV_{over}(T)}} = \mathrm{a}\ . \tag{7.23}$$

The PDE as a function of the overvoltage is approximated with a linear function shown in the right panel of Figure 7.4. Combining this assumption with Equation 7.17 results into

$$\begin{aligned} \frac{\mathrm{dQ(T)}}{\mathrm{dT}} &= \mathrm{A} \cdot \mathrm{B} \cdot \frac{\mathrm{dG(T)}}{\mathrm{dT}} + \mathrm{A} \cdot \frac{\mathrm{dB}}{\mathrm{dV_{over}(T)}} \cdot \frac{e}{\mathrm{C_D}} \cdot \frac{\mathrm{dG(T)}}{\mathrm{dT}} \cdot \mathrm{G(T)} \\ &= \left\{ 2\mathrm{a} \cdot \frac{e}{\mathrm{C_D}} \cdot \mathrm{G(T)} + \mathrm{b} \right\} \cdot \mathrm{A} \cdot \frac{\mathrm{dG(T)}}{\mathrm{dT}}\ . \end{aligned} \tag{7.24}$$

The charge at the reference temperature is

$$\mathrm{Q(T_{ref})} = \mathrm{A} \cdot \left\{ \mathrm{a} \cdot \frac{e}{\mathrm{C_D}} \cdot \mathrm{G(T_{ref})} + \mathrm{b} \right\} \cdot \mathrm{G(T_{ref})}\ . \tag{7.25}$$

Thereby the temperature coefficient of the SiPM charge can be written as

$$\begin{aligned} \alpha_\mathrm{r} &= \frac{\mathrm{dQ}}{\mathrm{dT}} \cdot \frac{1}{\mathrm{Q(T_{ref})}} = \frac{\mathrm{A} \cdot \left\{ 2\mathrm{a} \cdot \frac{e}{\mathrm{C_D}} \cdot \mathrm{G(T)} + \mathrm{b} \right\} \cdot \frac{\mathrm{dG(T)}}{\mathrm{dT}}}{\mathrm{A} \cdot \left\{ \mathrm{a} \cdot \frac{e}{\mathrm{C_D}} \cdot \mathrm{G(T_{ref})} + \mathrm{b} \right\} \cdot \mathrm{G(T_{ref})}} = \\ &= \left\{ 2 \frac{\mathrm{a} \cdot \frac{e}{\mathrm{C_D}} \cdot \mathrm{G(T)} + \mathrm{b}}{\mathrm{a} \cdot \frac{e}{\mathrm{C_D}} \cdot \mathrm{G(T_{ref})} + \mathrm{b}} - \frac{\mathrm{b}}{\mathrm{a} \cdot \frac{e}{\mathrm{C_D}} \cdot \mathrm{G(T_{ref})} + \mathrm{b}} \right\} \cdot \beta_\mathrm{ref}\ . \end{aligned} \tag{7.26}$$

With this model, there is indeed a temperature dependent factor between the two temperature coefficients. In order to approximate this factor, it is assumed that

$$\frac{\mathrm{G(T)}}{\mathrm{G(T_{ref})}} = 1.000 \pm 0.075\,;\ \text{if } \mathrm{T_{ref}} = 25\,^\circ\mathrm{C} \text{ and } \mathrm{T} \in \left[15\,^\circ\mathrm{C}; 35\,^\circ\mathrm{C}\right]\ , \tag{7.27}$$

which can be extracted from Figure 7.3. Together with Equation 7.26, this results into

$$\alpha_\mathrm{r}(\mathrm{T_{ref}}) = \left\{ 2 - \frac{\mathrm{b}}{\mathrm{a} \cdot \frac{e}{\mathrm{C_D}} \cdot \mathrm{G(T_{ref})} + \mathrm{b}} \right\} \cdot \beta_\mathrm{ref}(\mathrm{T_{ref}}). \tag{7.28}$$

With this transformation, the T dependency of the factor between α_r and β_r vanishes. The factor between the coefficients depends now only on $\mathrm{T_{ref}}$. Thereby $\alpha_\mathrm{r}(\mathrm{T_{ref}})$ fulfills the requirement that it is invariant in the temperature.

Note that, this model is consistent with the "Linear charge" model for the extreme case $\frac{\mathrm{dB(V_{over}(T))}}{\mathrm{dV_{over}}} = \mathrm{a} = 0$.

The “a” and “b” parameters of the linear function of the PDE dependency on the overvoltage can be estimated from Figure 7.4. With this estimation the theoretical calculated ratio of the temperature coefficients for the SiPM type S13360-1325PE equals $\frac{\alpha_r}{\beta_r}\Big|_{\text{theoretical}} = 1.39 \pm 0.09$, while the measured ratio is $\frac{\alpha_r}{\beta_r}\Big|_{\text{measured}} = 2.20 \pm 0.08$. The theoretical and measured values are not in agreement. The disagreement can be explained due to the lack of the precise values of the “a” and “b” parameters, and due to the simplified assumptions in the model such as that only the PDE parameter is temperature dependent. However, if the charge of the SiPM response contains at least one temperature dependent parameter, the temperature coefficient of the gain and the charge are not identical.

From the definition of the temperature coefficient, the charge could be determined by

$$\alpha_r(T_{ref}) = \frac{dQ}{dT}\frac{1}{Q(T_{ref})} \qquad \Big/ \cdot Q(T_{ref}); \int dT \tag{7.29}$$

$$Q(T) = \int Q(T_{ref}) \cdot \alpha_r(T_{ref})\ dT = Q(T_{ref}) \cdot \alpha_r(T_{ref}) \cdot T + \text{const} \ . \tag{7.30}$$

The charge of the SiPM response using the “Pseudo-quadratic charge” model has same linear form as used for the charge versus temperature calibration (Equation 7.2).

In summary, as the charge has further parameters with a temperature dependence in addition to the gain such as the Photo Detection efficiency, the temperature coefficients of the gain and the charge cannot be identical. An attempt was made to define the ratio of the two coefficients theoretically. A full agreement between theoretical and measurement values could not be achieved due to the limited knowledge of all temperature dependent variables of the SiPM charge.

Chapter 8

Tile scan results

One of the major motivations for the scintillator tile studies is given by the particle flow calorimetry, which requires highly segmented detectors on the hardware side as well as advanced reconstruction techniques on the software side 2.2.3. In this section, the results of the scintillator tile scans performed within the framework of this thesis work are discussed. The scintillator-SiPM response is here always corrected for the temperature dependence as introduced in Section 7.1. First, the single-tile measurements are discussed then the results of a multi-tile scan are shown in which the inter-tile crosstalk is evaluated.

8.1 Single-tile setup

In this section, the method of a single-tile scan and the corresponding evaluation will be introduced. Then, the measured light yield and uniformity of the light yield within the scintillator tile is compared between tiles of different coatings and sizes.

8.1.1 Method of the tile scans

In order to perform tile scans, the scintillator tile scan setup introduced in Section 3.3 is used. The tile is supported by a platform which is connected to stepper motors. The stepper motors move in 1 mm steps with respect to the electron gun and the trigger in two orthogonal directions. In order to study edge effects in the tile, an area bigger than the tile is scanned in all directions with approximately 3 mm in addition to the tile area. Since the surface of the studied tiles is between 1 cm^2 and 4 cm^2 and the measurement time is 100 s for each step, a full scan takes between 7 and 18 hours. During a full scan, the temperature varies by approximately 2 °C (see in Figure 8.1) caused by heat sources close to the setup and the day-night temperature fluctuations.

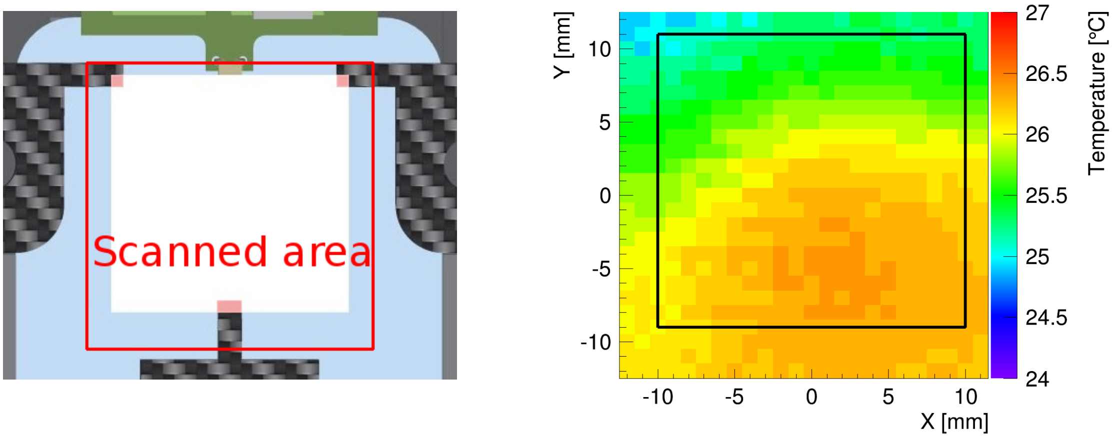

Figure 8.1: Left panel: An illustration of the direct environment of the tile. Highlighted are the direct contact between the tile holders and the tile. Right panel: The temperature map of a full tile scan. The temperature varied within a range of 2 °C.

This leads to approximately 3% difference in the charge (Section 7.1). To avoid the undesired effects of this temperature variation, the measured charge is corrected to a reference temperature of 25 °C using Equation 7.1.
Beside full tile scans, few tile slice scans are also performed, in which only the middle sections of the scintillators are scanned resembling a cross along the middle axes of the tile. With this approach, the time of the tile scan can be reduced to between 7.6% to 12.5% of the full tile scan.
The stable position of the scintillator tile is ensured by 3 tile holders. These holders are designed as part of this thesis work with low material close to the tile in order to avoid signals from stray electrons in the support structure in the tile.

8.1.2 Scintillator tiles

The material of the scintillator tiles is EJ-200 plastic [17] in all cases. The scintillator tiles used in this study have three features for identification:

1. Batch number: this number corresponds to the date of production. There are three batches in use 1, 2 and 3. The oldest batch has the lowest number.

2. Coating: the naked scintillator material is covered with one of two different coatings. One possibility is to wrap the tiles with a 3M reflection foil [18]. Both perfection in the fixation of the foil to the tile's surface is reproducibility are limited. Between the foil and the scintillator material, an air-gap can occur which can lead to total reflection of the photons.

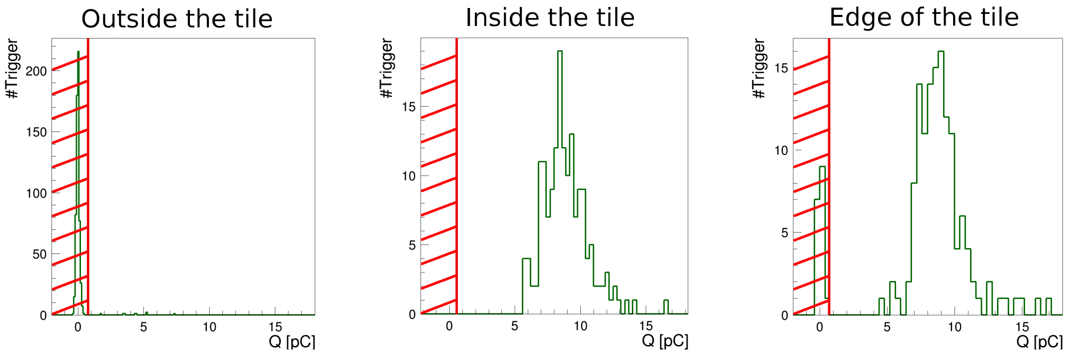

Figure 8.2: Left panel: The pedestal peak recorded outside the tile. Middle panel: The Landau Gauss convolution measured in the interior of the scintillator. Right panel: The beam penetrates at the edge of the tile, therefore the mixture of the distributions outside and inside the tile appears in the charge spectrum. All three charge distributions are displayed in the signal-pedestal sub-window. The red shaded area indicates the rejected area.

The second coating is a reflective paint material [19]. The advantage of the painting is that it can be distributed homogeneously on the surfaces of the tile.

3. Size: all tiles have a square-shape based cuboid with 2 mm height. The edge length of the squares is 10 mm, 15 mm and 20 mm.

In the following a naming scheme based on the characteristics is used to identify the scintillator tiles. For example a tile from batch 1, with 3M wrapping and with $20 \times 20 \times 2\,\mathrm{mm}^3$ size is named B1W20. In addition, a serial number is added to the name, which can be found on the tile itself (for instance: batch 3, 3M wrapping, with $20 \times 20 \times 2\,\mathrm{mm}^3$ size, serial number 1 = B3W20N1) for tile types where more than one tile exists.

8.1.3 Regions of a tile scan

The electron beam used for the tile scans traverses a collimator in the electron monochromator introduced in Section 3.3. The size of the electron beam relevant for the tile scan is further reduced by the acceptance window of the trigger fibers with an overlap region of $1 \times 1\mathrm{mm}^2$. The diameter of the beam shape on the tile is therefore $\varnothing 1$ mm. Due to the significant electron beam size with respect to the tile dimensions and step size, three tile positions with respect to the beam can be identified. Therefore, the electron beam divides the scanned area (see in Figure 8.2) into three regions:

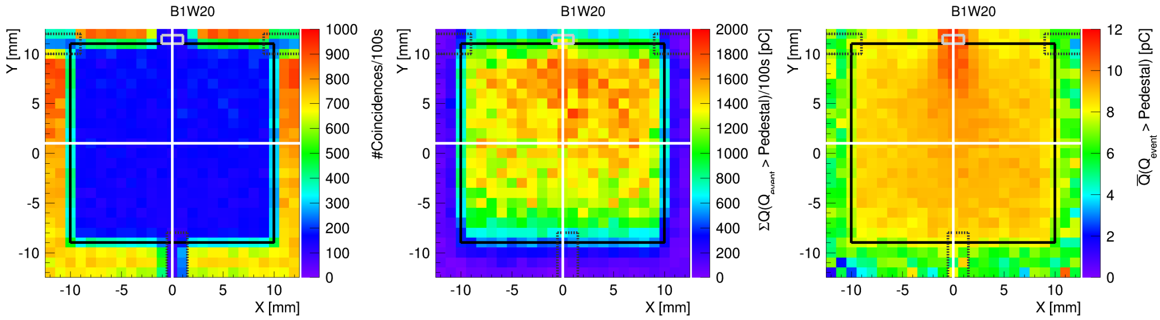

Figure 8.3: The 2D distributions of the B1W20 tile are shown. Left panel: The number of coincidences in 100 s. Middle panel: The integrated charge for 100 s. Right panel: The average charge.

1. all e^- do not traverse the tile
2. all e^- traverse through the tile
3. the e^- beam is on the edge of the tile such that some electrons traverse through the tile and some do not.

In the 1st case, the electron beam does not interact with the scintillator, the SiPM response only contains noise. The recorded signal peaks are at 0 pC. In the 2nd case, the whole electron beam penetrates through the scintillator tile, which leads to a Landau Gauss convoluted charge distribution (described in Section 4.1.2). The 3rd case contains both distributions since it is a mixture of the first two cases. Since the measurements are focused on the investigation of the physical processes between the electrons and the scintillator tile, the pedestal distribution is rejected for each step from the signal-pedestal sub-window in all regions. The rejection is realized through a removal of all events below a value of $\sqrt{2} \cdot 3 \cdot \mathrm{STD}_{\mathrm{pedestal}}$ that is measured simultaneously in the pedestal sub-window.

8.1.4 Evaluation of the collected charge

After the event selection introduced in Section 8.1.3, three two dimensional distributions are defined for the evaluation of the tile scans. In all 2D distributions, the horizontal and vertical axes comply with the xy plane of the tile scan setup and are parallel with the long edges of the investigated scintillator tiles. The SiPM is located at the middle top, the three tile holders are at both top corners and the middle of the bottom edge of the tile.

The first observable shown in the left panel of Figure 8.3 for wrapped 20×20 tile,

indicated in the vertical axis shown in color code, is the number of coincidences (number of triggers) during the measurement time for each step of 100 s each. Since the step size of the scans is 1 mm, the coincidence map is used as a crosscheck of the alignment as well as a crosscheck of the scintillator uniformity. Air bubbles or holes would show up as an increased number of triggers.
The second vertical observable is the integrated charge shown in the middle panel of Figure 8.3. In this case, all charge collected for the measurement time in one step is summed up. The map allows the separation of the border between the scintillator tile and the empty area, thereby it can be used to understand better the effects at the edges of the scintillator tile. The third observable is the mean of the collected charge for the measurement time in one measurement point shown in the right panel of Figure 8.3. The MPV of the Landau Gauss convolution introduced in Section 4.1.2 can not be used at the edge of the tile and the outside region of the tile due to the limited number of events selection as discussed in Section 8.1.3. The mean of the charge equals the integrated charge normalized the number of coincidences. In this distribution the borders of the tile are not visible. However, the map is used for comparing the light yield of different tiles to each other.

In the top rows of Figure 8.4 and 8.5 slices of these two dimensional distributions at y = tile middle in x-direction are shown and, in the bottom rows slices at x = tile middle in y-direction are shown for all tested tile types. The $20 \times 20 \times 2\,\text{mm}^3$ sized tiles displayed in red colors, the $15 \times 15 \times 2\,\text{mm}^3$ sized tiles is displayed in green colors and the $10 \times 10 \times 2\,\text{mm}^3$ sized tile is displayed in blue colors. All slices are measured twice, in order to check the reproducibility of a tile scan. The systematic uncertainty shown in Figure 8.4 contains the uncertainty of the reproducibility of a tile scan with replacement and the uncertainty of the reproducibility depending on the number of triggers of the charge measurement itself (Section 5.2.3). The bands represent the statistical and the systematic uncertainties summed up by the rules of the Gaussian error propagation. The lines and bands between the measurement points are for guiding the eye.
For the x and y coordinates in which the electrons do not traverse the tile, the coincidence rate increases by a factor of 5 to 6. Inside the tile, the number of triggers for 100 s is relatively constant with fluctuations compatible with $\mathcal{O}(\sqrt{\text{Trigger}})$. The number of triggers in y-direction do not increase at the tile edges. There, the electrons traverse through material of the support structure before they reach the trigger fibers. For positive y-values outside the tile edge at the tile middle, the tile is coupled

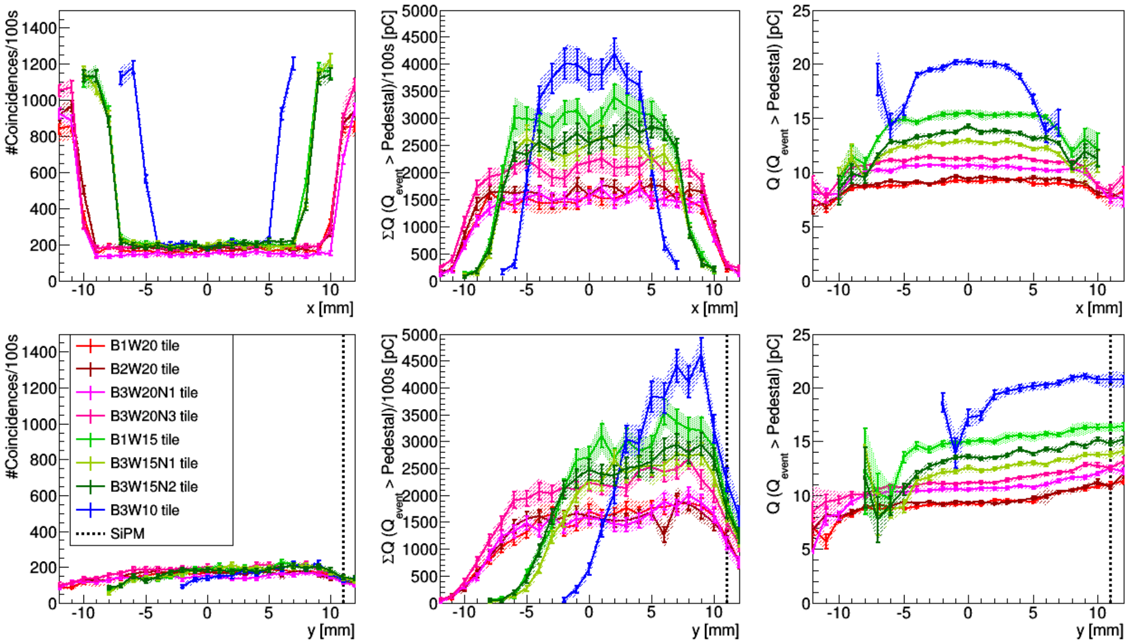

Figure 8.4: The results of the tile cross sections are shown for the wrapped tiles. Left panels: Number of coincidences. Middle panels: Sum of the charge. Right panels: Average charge.

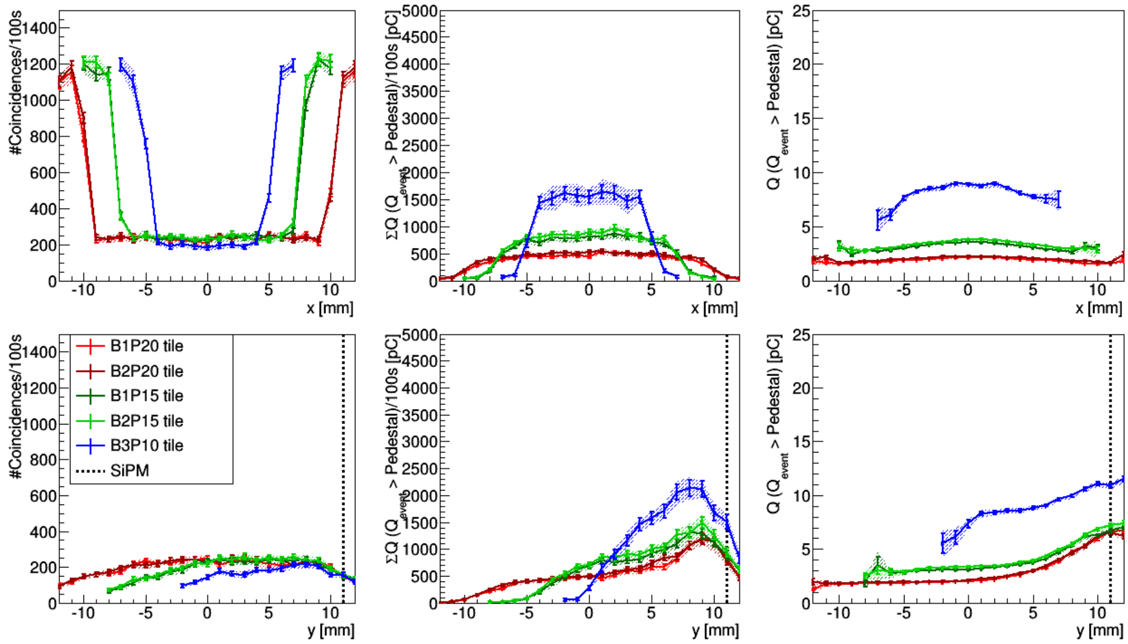

Figure 8.5: The same distributions are shown here as in Figure 8.4 for the painted tiles.

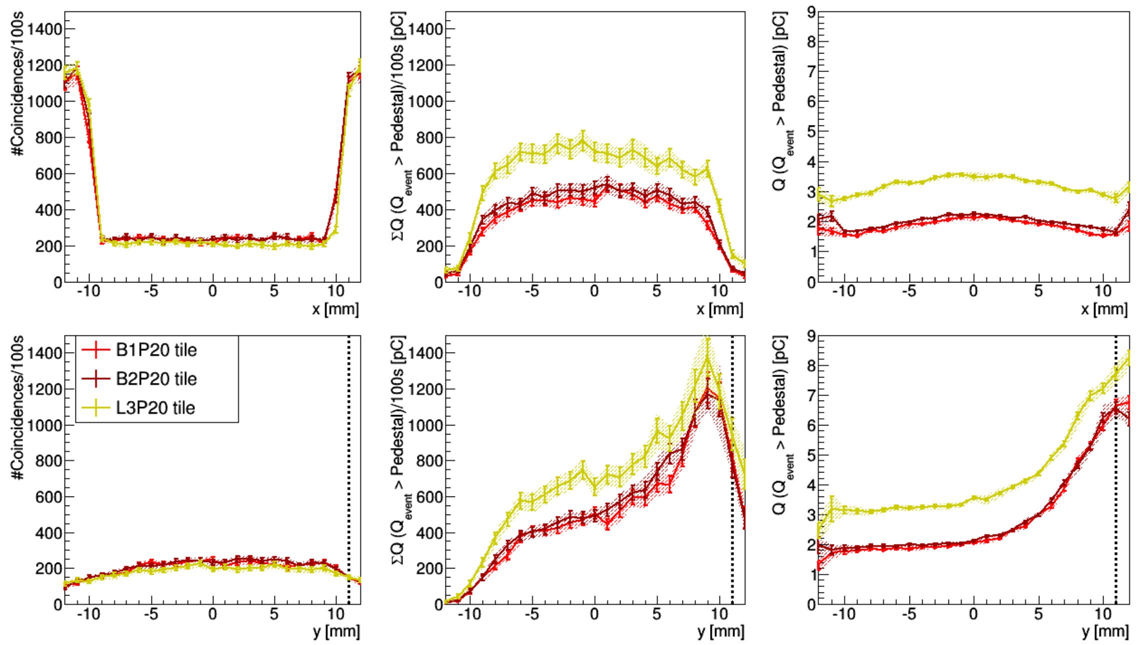

Figure 8.6: Comparison between tiles with one layer of paint and 3 layers of paint. Left panels: Number of coincidences. Middle panels: Sum of the charge. Right panels: Average charge.

to an SiPM and for negative y-values outside the tile edge at the tile middle; the tile is supported by a tile holder as shown in the left panel of Figure 8.1.
The integrated charge shown in the mid panel of Figure 8.4 shows similar fluctuations as the number of triggers. Approximately 1-2 millimeters before the tile edge in x-direction and approximately 5 mm before the tile edge in negative y-direction the integrated charge starts to decrease. In addition, a peak appears in the integrated charge which has its maximum a few millimeters before the SiPM. This effect is particularly significant in the case of the painted tiles (Figure 8.5), and is less significant for the wrapped tiles (Figure 8.4). The light yield of the wrapped scintillators scales with the sizes of the tile such that the light yield of these tiles is proportional to the covered area by the SiPM to the tile's front surface, as shown in Table 8.1. The values are calculated both for homogeneous (hom. = tile area without the peak in the charge distribution and without the edges) and total scanned area of the tiles. The mean light yields of the wrapped tiles of same size differ to each other by 22% in the case of the $20 \times 20 \times 2\,\text{mm}^3$ and by 20% in the case of the $15 \times 15 \times 2\,\text{mm}^3$ sized tiles. This variation can be explained by the limited reproducibility of the fixation of the foil to the tile surface.

Table 8.1: The average light yield ratio (a. l. y.) of the wrapped tiles of different sizes. The light yield of the tile is proportional to the covered area of the SiPM with respect to the tile's front surface.

	W15÷W20	**W10÷W15**	**W10÷W20**
side surface ratio	1.33	1.5	2
a. l. y. ratio (hom.)	1.39±0.39	1.43±0.25	1.99±0.48
a. l. y. ratio (total)	1.37±0.64	1.42±0.43	1.95±0.78

Table 8.2: The average light yield (a. l. y.) ratio of the painted tiles of different sizes. The light yield of the tile is not proportional to the covered area of the SiPM with respect to the tile's front surface as in the wrapped tile cases Table 8.1.

	P15÷P20	**P10÷P15**	**P10÷P20**
side surface ratio	1.33	1.5	2
a. l. y. ratio (hom.)	1.74±0.41	2.55±0.41	4.44±0.97
a. l. y. ratio (total)	1.52±0.63	2.43±0.66	3.70±1.37

The light yield ratio for the painted tiles differs from the ratio caused only by the tile's side area ratio showed in Table 8.2. This effect can be explained due to the higher photon-absorption rate of the painting material compared to the wrapping material with photon-absorption approximated by 1 resulting to unequal relative number of photons normalized for the tile size arriving to the SiPM's active area. However, the average light yield is more similar for painted tiles of same size (within $4\% - 6\%$) than for wrapped tiles (approximately 21%). It can be explained due to the fact that the painting distributed more homogeneously on the tiles surfaces. The average light yield of the painted tiles for $20 \times 20 \times 2\,\mathrm{mm}^3$ tile is 24%, for $15 \times 15 \times 2\,\mathrm{mm}^3$ tile is 27% and for $10 \times 10 \times 2\,\mathrm{mm}^3$ tile is 46% with respect to wrapped tiles of same size. The normal painted tiles are covered by one layer of paint. To increase the light yield, one tile (L3P20) has been produced with three layers of reflective painting. As shown in Figure 8.6, the additional two layers of paint increase the average light yield of the tile by approximately 56%.

8.1.5 Uniformity

In this chapter, the uniformity of the scintillator tiles' response is investigated using the data of the integrated charge. In the case of the B1W20, B2P15 and L3P20 tiles full tile scans are performed. For the remaining tile set cross sections in the tile middles along x and y coordinates are available. Using the informations of the full

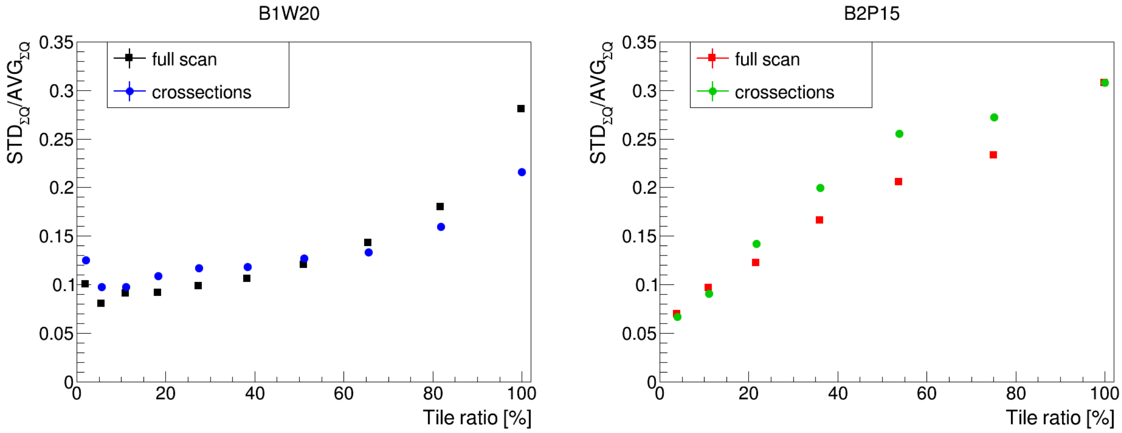

Figure 8.7: The uniformity of the B1W20 tile (left) and the B2P15 tile (right) is studied both for the full tile scan and for the tile cross section case.

scans the uniformity is studied using the standard deviation (STD) over the average of the integrated charge ($STD_{\Sigma Q}/AVG_{\Sigma Q}$) in the investigated area. The uniformity scales reciprocal with the $STD_{\Sigma Q}/AVG_{\Sigma Q}$. The tile is highly uniform for low $STD_{\Sigma Q}/AVG_{\Sigma Q}$ values and vice versa. The same calculation is performed using the cross section data sets.

In order to investigate the uniformity of substructures of the tiles, the uniformity is calculated for sub-areas of a tile. These sub-areas are referred to with a ratio with respect to the full tile size called as "tile ratio". The center of these sub-areas always matches the center of the full tile. The sub-areas are square-shaped for the full scans, and the cross section datasets for certain tile ratio are made of the cross sections within the square-shaped sub-areas.

In Figure 8.7, the $STD_{\Sigma Q}/AVG_{\Sigma Q}$ distribution of the full scanned area and of the tile cross section as a function of the tile ratios are shown for the B1W20 tile (left panel) and for the B2P15 tile (right panel). The dataset calculated from the cross section measurement follows the dataset of the full tile scan, but fluctuates around the full tile scan result due to its lower statistic. The two methods does not agree within the uncertainties, the maximum difference is 6.5%. Therefore, for further studies the uniformity is represented by the $STD_{\Sigma Q}/AVG_{\Sigma Q}$ of the tile cross sections available for all tile types with a systematic uncertainty of 6.5%.

In Figure 8.8 the uniformity distributions of the cross section data are shown as a function of the tile ratio for the full tile set. All tiles are measured twice, the difference between the two measurements are shown as systematic uncertainties as bands. The continuous lines and bands between the data points are for eye-guiding.

Three different data groups can be identified. The highest $STD_{\Sigma Q}/AVG_{\Sigma Q}$ values

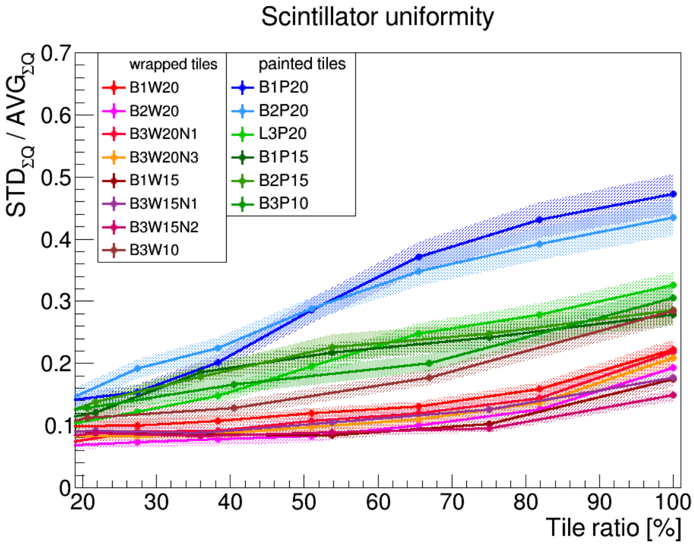

Figure 8.8: The uniformity as a function of the tile ratio for all tiles.

(lowest uniformity) belong to the tiles with lowest integrated charge which are the biggest painted tiles, marked with blueish colors. The second group comprises the smaller painted tiles with higher integrated charge and with higher uniformity, marked with greenish colors. This group also contains the special L3P20 tile (introduced in the end of Section 8.1.4) which has 3 layers of paint on its surface resulting similar integrated charge level and similar uniformity as for the painted $15 \times 15 \times 2\,\mathrm{mm}^3$ tiles. The third group contains all wrapped tiles with high integrated charge and with the highest uniformity, marked with reddish colors. These three groups of tiles in uniformity appears, since for high integrated charges within a tile the peak in the integrated charge a few millimeters before the SiPM exceeds slightly while for lower integrated charges the peak become dominating causing low uniformity. However, the tile size also plays role in the tile uniformity. Since the range of the edges within a tile and the area of the peak before the SiPM stay approximately constant with the tile size (Figure 8.4 and 8.5), the homogeneous area within the tile gets bigger with the tile size. This results to higher differences in the integrated charge for smaller tile sizes, hence, to lower uniformity. The lower uniformity of the B3W10 and B3P10 tiles can be explained by this effect. Regarding their level of the integrated charge, both uniformity distributions should reach the level of the tiles with high uniformity (reddish band). But their integrated charge distribution within the tile is more inhomogeneous due to the small size, their uniformity distributions extend into the middle uniformity group (greenish band).

Based on Figure 8.8, with such a sub-area placement the uniformity of a tile has a reciprocal connection with the tile ratio.

8.2 Multi-tile setups

In the following results of multi-tile scans will be shown. The multi-tile measurements have the purpose to help to better understand edge effects at the contact of tiles and the crosstalk effects between tiles, crosstalk has an impact on the energy scale of a calorimeter [7].

8.2.1 Realization of the multi-tile setups

Two kinds of multi-tile setups are established. The design of both setups is based on similar principles as in the single-tile setup case. The tile(s) should be positioned stably while the holders have to interact with the tile(s) as less as possible in order to avoid strayed electrons from the support structure in the tile. In addition the support should allow for an easy placement and replacement of all tiles with different sizes. Considering all these aspects, a 2-tile setup and a 4-tile setup were prepared as part of this study with 3D printing technology. The corresponding CAD drawings are shown in Figure 8.9.

For the easiest realization, the SiPMs are placed opposite in the 2-tile setup. In the 4-tile setup the SiPMs are rotated by 90 ° with respect to the position on the neighboring tile. The setups allow the placement of maximal 2 PCBs for the signal amplification for each SiPM. To use additional SiPMs, the Data Acquisition software implemented in LabView needs some modifications: in the 2 tiles case one PicoScope with 4 read out channels can handle the second SiPM. In the 4 tiles case a second PicoScope is required. These setups allow for the investigation of the crosstalk between scintillator tiles. The crosstalk can be realized due to photon leakage between the neighboring tiles, but also due to strayed electrons from an adjacent material.

8.2.2 Results of the 2-tile scan

In the following, 2-tile scan measurements are presented with one SiPM connected to one of the two scintillator tiles. The tile holders are placed in the same way as presented in Figure 8.9 in the left panel. The tile which is read out by the SiPM under study is the B1P15 tile and the second tile is B2P15. The light yields of these tiles studied in Section 8.1.4 are in agreement within the uncertainties.

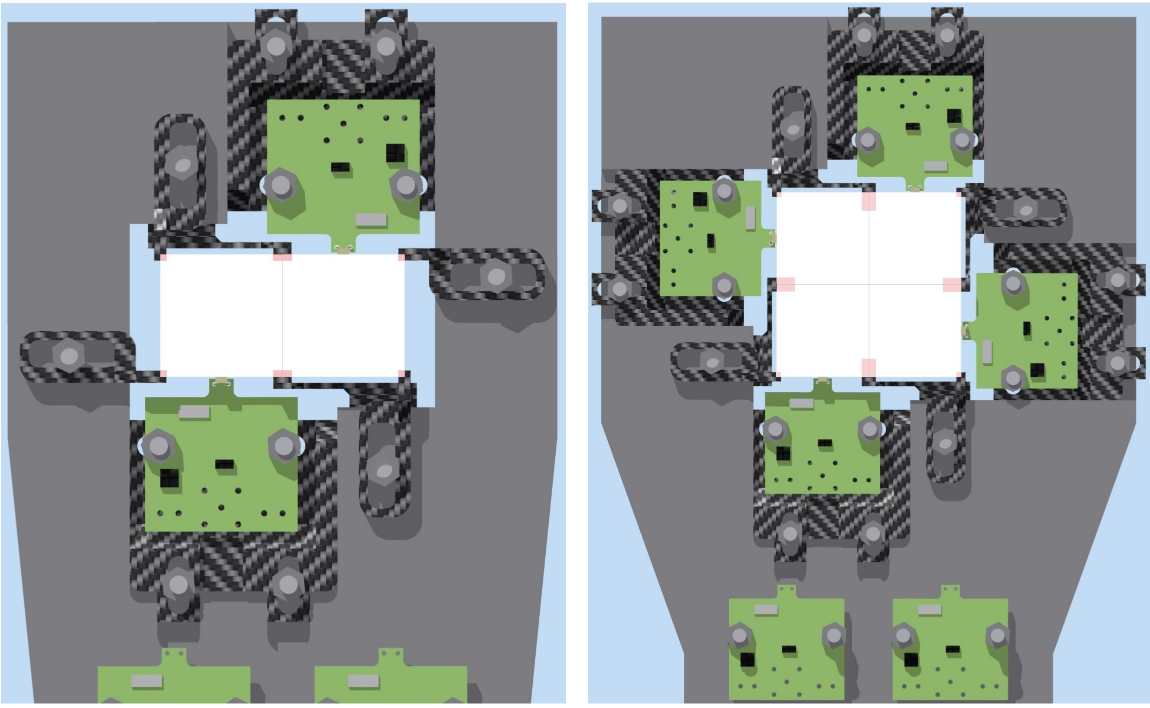

Figure 8.9: The multi-tile setup with their close environment around the tiles. The 2-tile setup is displayed on the left, the 4-tile setup is on the right. In both panels the red ranges indicate the interaction surfaces between the tiles and the their holders.

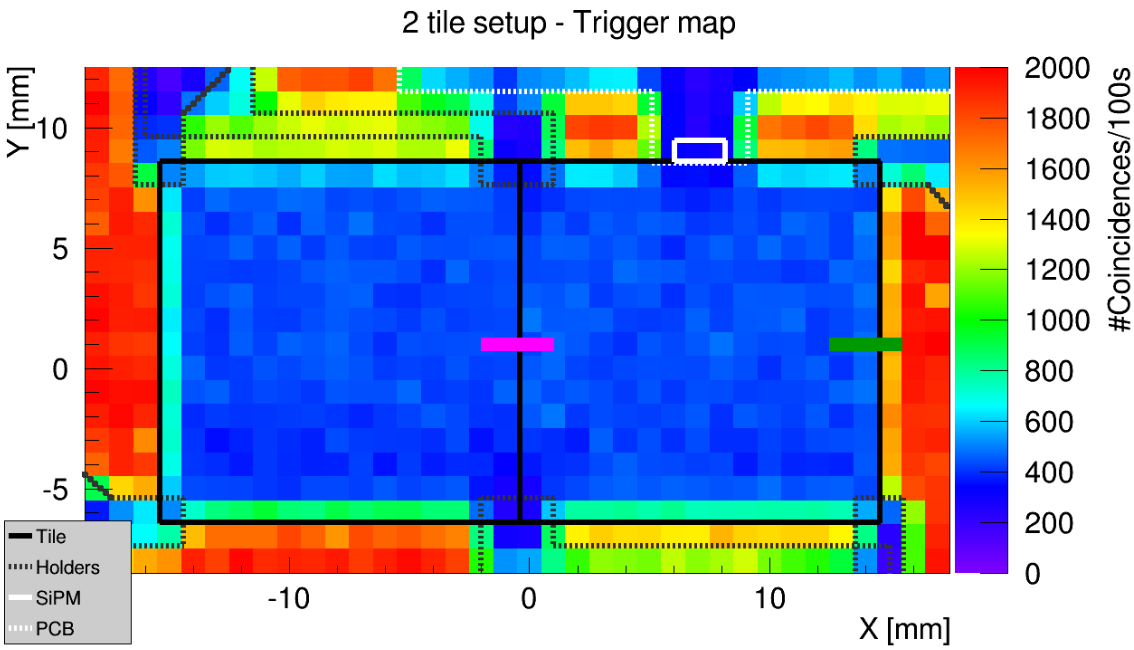

Figure 8.10: The number of coincidences map of the 2-tile setup. The presence of the tile supports and the PCB, SiPM is reflected in the reduced number of coincidences.

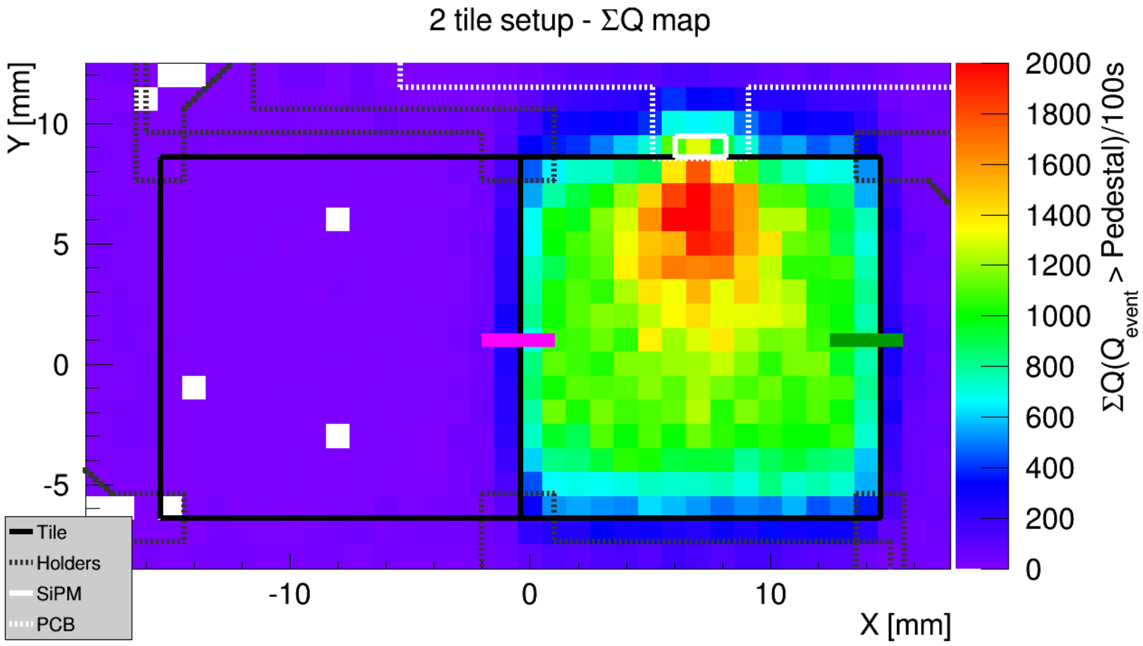

Figure 8.11: The integrated charge map of the 2-tile setup. In order to study the effects at the edges of the scintillator, a measurement was performed with smaller steps size in the middle line in x-direction indicated as wide magenta and dark green colored lines. The wide magenta and dark green colored lines mark the positions of two scanned slices with decreased measurement steps.

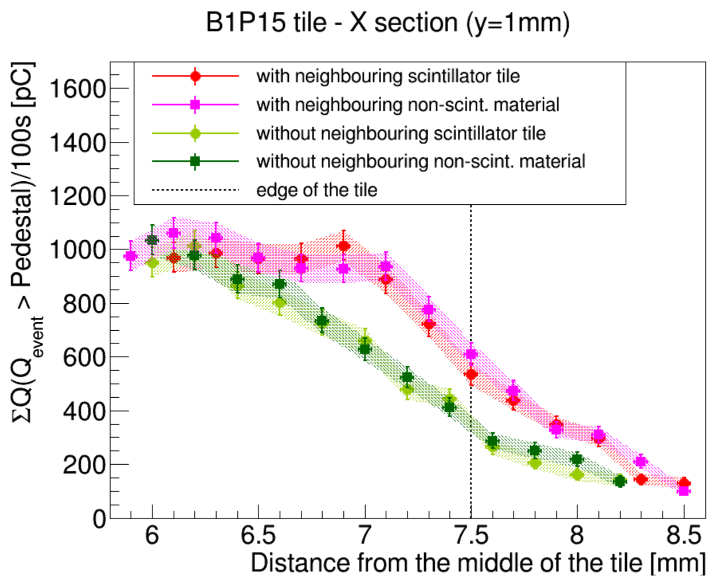

Figure 8.12: The integrated charge as a function of the distance from the middle of the tile. The figure is based on the measurement using a scintillator placed next to the read out tile and the measurement using non-scintillator material next to the read out tile.

In Figure 8.10, the number of coincidences map of the 2-tile scan is shown. The presence of the tiles itself, the tile support system, the PCB and the SiPM is reflected in the reduced number of coincidences. In Figure 8.11, the integrated charge map of the 2-tile scan is presented.
To investigate the transition region between the two tiles in detail, approximately at the middle in y-direction two slices are made scanning in x-direction with decreased measurement step size of 0.2 mm. These slices are indicated as wide magenta and dark green colored lines in Figure 8.10 and in Figure 8.11. In addition, a second measurement is performed, where the second scintillator tile is replaced by a non-scintillating plastic material, which does not produce photons.

In Figure 8.12, the integrated charge is shown as a function of the distance from the middle of the scintillator tile. The dataset at the tile edge next to non-scintillating material (green color) is in agreement with the dataset at the tile edge next to scintillator material (red and magenta color) while both datasets differ from the one at the edge next to air. In addition, the two measurements at the tile edge without adjacent material agree. Based on these measurements, the difference in the collected charge does not correspond to light leakage but to strayed electrons from the neighboring material.

To get a better understanding of the light crosstalk independent of stray electrons, the setup can be equipped with LEDs shining light only in one tile. The measurement with this extension is already allowed by the design of the tile holders, but goes beyond the scope of this thesis. Measurements of the crosstalk found that the crosstalk factor is 2.5% [31] and between 3.3% and 4.6% [32] of the total energy per edge for cells with size of $3 \times 3\text{mm}^2$.

In Figure 8.13, the $z-$coordinates within the secondary scintillator tile represent how much summarized charge is generated in the SiPM due to electrons strayed from the secondary tile to the primary tile at the sub-area level compare to the summarized charge in the same sub-area of the primary tile. The rate of these events within a tile strongly depends on the position, it decreases dramatically with the distance from the neighboring edge of the scintillator tiles. The integrated charge caused by such events compared to the integrated charge of the primary tile for the overall tile area is $(2.1 \pm 1.5)\%$ in the case of the 2-tile setup and $15 \times 15 \times 2\,\text{mm}^3$ tiles using an electron beam with size of approximately $\varnothing 1\,\text{mm}$.
The final energy threshold increases with the crosstalk rate on the energy scale of a calorimeter, since the leaked signal into neighboring tiles can cause signals above

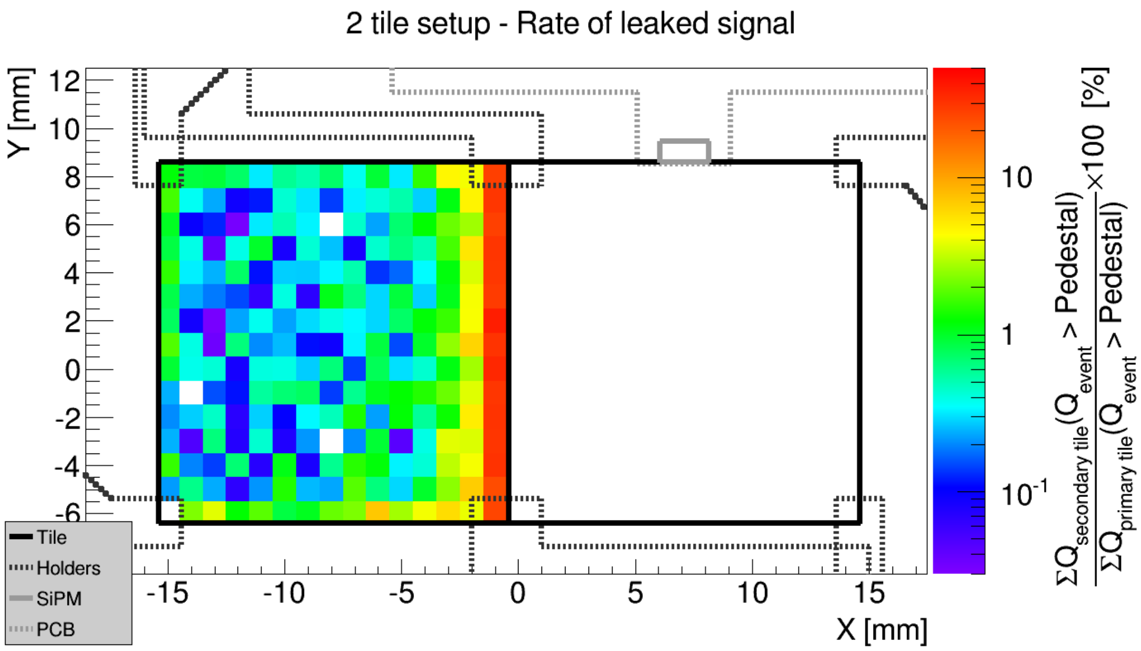

Figure 8.13: The 2D distribution of the leaked signal at the sub-area level of the scintillator tile.

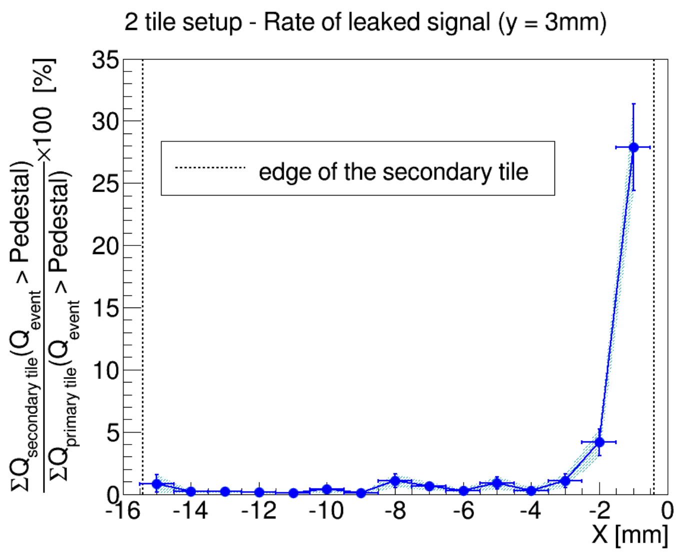

Figure 8.14: The section in x direction at $y = 3\,\text{mm}$ of the leaked signal distribution showed in Figure 8.12. The rate of the leaked signal decreases dramatically with the distance from the meeting edge of the scintillator tiles.

Table 8.3: The results of the tile investigations are summarized here. The wrapped tiles has higher amount of light yield and have more uniform response within a tile, while the mass production and the placement of the painted tiles are much easier and the painted tiles has better intertile-uniformity.

	Wrapped tiles	**Painted tiles**
Coating evenness (intertile-uniformity)	uneven wrapping $\Rightarrow$ inhom. light containment $\Rightarrow$ inhom. photon-reflection $\Rightarrow$ 21% uncert. in a.l.y.	homogeneous painting $\Rightarrow$ 5% uncert. in a.l.y.
Mass production	difficult	easy
Light yield level	high light yield	27% – 46% light yield of the wrapped tiles for one layer, 37% for 3 layers
Uniformity	high uniformity	low uniformity: $\frac{\text{STD}_{\Sigma\text{Q}}}{\text{AVG}_{\Sigma\text{Q}}}\Big\|_{p.} \sim 2 \times \frac{\text{STD}_{\Sigma\text{Q}}}{\text{AVG}_{\Sigma\text{Q}}}\Big\|_{w.}$
Light containment	sufficient separation	sufficient separation
Placement	difficult	easy

threshold. For a good determination of the energy scale the uncertainty of the leaked signal rate need known.

8.3 Recommendation

In this section a brief summary is given regarding the scintillator tiles based on the results discussed in the single-tile and multi-tile sections. In addition, a scintillator tile type recommendation is given for future applications.
It should be noted that different cover for the scintillator tiles or different SiPM placement to the tile can provide also an interesting alternative for scintillator tile studies as for instance the studies of the CALICE collaboration like [31] and [33].

The results of the tile investigations are summed up in Table 8.3. The first main category for the comparison of the coating materials is named "coating evenness". The uncertainties in the average light yield (δ(a.l.y.)) between scintillator tiles with same specifications are related with the coating type. The δ(a.l.y.) is proportional reciprocally with the intertile-uniformity, which characterize the similarities in the average light yield between tiles with same specifications but with different production number. The preparation of the wrapping needs precise technique which is nor optimal for mass production. In addition, the placement of the reflective foil leads to inhomogeneous light containment. The inhomogeneous light containment entails systematically inhomogeneous photon-reflections at the tile tile surface, thereby leads to lower intertile-uniformity. The dye material of the painted tiles can be distributed much more homogeneously than the reflective foil, therefore leading to better intertile-uniformity: $\delta(\text{a.l.y.})\big|_{\text{wrapping}} \approx 4 \times \delta(\text{a.l.y.})\big|_{\text{painting}}$ (see Section 8.1.4 for details). The mass production and the alignment of the tile in a detector is more easier in the painted tile cases. Both points play an important role for the production of a large scale calorimeter.

The next category is the light yield level of the tiles (see Section 8.1.4). The light yield level (l.y.l.) of the wrapped tiles differ significantly to the light yield level of the painted tiles: $\text{l.y.l.}\big|_{\text{painting}} \approx (27\% - 46\%) \times \text{l.y.l.}\big|_{\text{wrapping}}$. However, this difference in the light yield levels can be partly equalized by covering a tile with more layers of painting. This reduces the difference to 37% for the 20×20 sized tiles.

The uniformity investigated in Section 8.1.5 measures the uniformity within a single tile, while the intertile-uniformity means the uniformity between tiles with same specifications but with different production number. The uniformity within a tile is better for the wrapped tiles than for the painted tiles. The difference scales approximately with a factor two and primary caused by the peak in the measured charge at few millimeters before the SiPM active surface. This peak is more outstanding by comparison to the average charge within the painted tiles than within the wrapped tiles. However, the size of this peak in the measured charge can be changed by machining a slit and an integration hole for the SiPM into the scintillator material as discussed in [34]. With this method the uniformity of the scintillator response can be improved [34] and this technique is already used in the new CALICE AHCAL prototype [35].

The light containment of both coatings is sufficient to avoid photon leakage from neighboring tiles as shown in Section 8.2.2.

Table 8.3 does not contains the tile sizes, their influence is summarized in this paragraph. Independently on the coating smaller tile size corresponds to higher light yield within a tile. Based on the studies interpreted in Section 8.1.5, there are two counteractive effects on the uniformity depending on the tile size. If the tile size is big, the light yield level of the tile becomes low, the presence of the peak in the charge before a few millimeters the SiPM decreases the uniformity. But if the tile size is small the edge effects start to dominate within the tile resulting also lower uniformity. These two effects result that the middle sized tiles ($15 \times 15\,\text{mm}^2$) have the highest uniformity within the studied tile sets.

In summary, the painted tiles fulfilled more categories in Table 8.3 than the wrapped tiles. The advantages of using paint as coating of a scintillator are the easy mass production, the homogeneous distribution of the paint on the tile surface, the easy placement of the tile and the sufficient light containment. The most important disadvantage compared to the wrapping is the lower light yield. However, the light yield can be increased by using more layers of paint. The negative effect of the peak in the charge distribution at a few millimeters before the SiPM on the tile uniformity can be decreased with the techniques introduced in [34]. Taking all the above mentioned considerations into account, it is suggested to use of a tile with reflective paint coating on its surface with size of $15 \times 15 \times 2\,\mathrm{mm}^3$ or with size of $10 \times 10 \times 2\,\mathrm{mm}^3$, which meets with the requirement of the particle flow technique [8].

Chapter 9

Summary

In this thesis, SiPM and scintillator studies for applications in sampling calorimeters of future multi-TeV e^+e^- colliders such as the Compact Linear Collider (CLIC) are described. First the working principle of the SiPM and the scintillator tile were introduced. Two measurement setups for SiPM gain calibrations and for scintillator tile scans were described. For the investigations an SiPM with type Hamamatsu MPPC S13360-1325PE and a plastic scintillator tile set with different sizes and coatings (wrapping, painting) were used.
The SiPM calibrations was described including the overvoltage calibration, the gain vs. temperature calibration ($\beta_{\mathrm{r}}(\mathrm{T}_{\mathrm{ref}})$) and the charge vs. temperature calibration using scintillator tiles ($\alpha_{\mathrm{r}}(\mathrm{T}_{\mathrm{ref}})$). The temperature coefficients obtained from both temperature calibrations, for the same SiPM under study differed by a factor of approximately 2. An attempt was made to describe the reason of this effect which is done to additional temperature dependencies in the charge measurement and to find a conversion between the two coefficients.
Applying the charge-temperature calibration results, scintillator tiles with different sizes and coatings were scanned using an electron beam. The scintillator tiles were studied in terms of the number of triggers, the integrated charge and the average charge for the measurement time in one scan step. The studies showed that the light yield for the wrapped scintillator scales with the sizes of the tile, i.e. the light yield of the wrapped tiles are proportional to the covered area of the SiPM to the tiles front surface. The light yield of the painted tiles was only $20\% - 25\%$ of the wrapped tiles. The tiles covered by reflective paint with the same size had more similar average light yield (within 7% variation) than in the case of the wrapped tiles with the same size (approximately 20% variation). The painting thickness had a significant impact for the light yield. Using 3 layers of paint instead of the 1 layer paint resulted in 68% more light yield with respect to 1 layer of paint.

Last but not least, initial studies of a 2-tile setup were shown, which had the purpose to better understand of crosstalk effects between the scintillators which could affect the energy scale in the full detector. In the 2-tile setup a primary and a secondary painted scintillator tiles of same size were placed next to each other and the light produced in the primary scintillator was read out with an SiPM. The presence of the secondary tile had an impact on the light yield of the primary tile. Based on the measurement presented in this study this impact was governed by electrons strayed from the material of the secondary tile not by photons leaking from one tile to the other. As an extension for additional studies of the crosstalk, the setup can be equipped with LEDs shining light only in one tile, which is already allowed by the design of the multi-tile setups.

Acknowledgements

First of all, I would like to thank Dr. Lucie Linssen as the CERN PH-LCD group leader for giving me the opportunity to come to CERN as a technical student and to participate in the work of the group.
Also, I would like to acknowledge Dr. Eva Sicking for her tireless supervising, especially for her teaching in the field of computer analyzing methods and Dr. Wolfgang Klempt, who provided me many technical advices for the implementation of the measurements.
In addition, I would like to thank the CERN Linear Collider Deterctor group for their help especially Magdalena Münker, Dr. Andreas Nürnberg, Dr. Dominik Dannheim and Dr. Konrad Elsener.
Last but not least, thank my family for the support and for the lots of patience.

Bibliography

[1] M. J. Boland et al. Updated baseline for a staged Compact Linear Collider. 2016. DOI[10.5170/CERN-2016-004].

[2] M. Aicheler et al. A Multi-TeV Linear Collider Based on CLIC Technology. 2012. DOI[10.5170/CERN-2012-007].

[3] P. Lebrun et al. The CLIC Programme: Towards a Staged e^+e^- Linear Collider Exploring the Terascale : CLIC Conceptual Design Report. 2012. DOI[10.5170/CERN-2012-005].

[4] A. Tehrani et al. CLICdet: The post-CDR CLIC detector model. Nov 2016. CLICdp-Draft-2016-025.

[5] S. Sroka, W Klempt. New CLIC detector model - engineering input to the tracker layout. 2016. EDMS document No. 1706383.

[6] E. Sicking. Particle flow calorimetry. DPG Spring Meeting 2016, Hamburg. URL: `https://twiki.cern.ch/twiki/pub/CLIC/DpgSpring2016/eva_sicking_particle_flow.pdf`.

[7] The CALICE Collaboration. Shower development of particles with momenta from 15 GeV to 150 GeV in the CALICE scintillator-tungsten hadronic calorimeter. *Journal of Instrumentation*, 10(12):P12006, 2015. URL: `http://stacks.iop.org/1748-0221/10/i=12/a=P12006`.

[8] S. Green, B. Xu, J. Marshall, M. Thomson. ILD Optimisation Studies. CLIC Detector and Physics Collaboration Meeting 30-31 August 2016 CERN. URL: `https://indico.cern.ch/event/487219/contributions/2275661/attachments/1329104/1996494/CLICdpWorkshop_OptimisationStudies_Green.pdf`.

[9] J. S. Marshall and M. A. Thomson. Pandora Particle Flow Algorithm. The Pandora software development kit, CHEF 2013. (AIDA-CONF-2015-004), Apr 2013. AIDA-CONF-2015-004.

[10] D. Dannheim, T. Frisson, S. Kulis. Lab Experiment: Characterization of Silicon Photomultipliers, November 2013. Danube School. URL: http://cern-danube-school.uns.ac.rs/assets/labs/Lab%207_SIPM.pdf.

[11] S. Piatek. Hamamatsu - Physics and Operation of an MPPC. 2016.02. URL: http://www.hamamatsu.com/us/en/community/optical_sensors/tutorials/physics_of_mppc/index.html?utm_source=googleplus&utm_medium=social&utm_campaign=hc-social#header.

[12] D. Renker and E. Lorenz. Advances in solid state photon detectors. *JINST*, 4(2009):P04004, 2009. DOI[10.1088/1748-0221/4/04/P04004].

[13] E. Garutti. Silicon photomultipliers for high energy physics detectors. *JINST*, 6:C10003, 2011. DOI[10.1088/1748-0221/6/10/C10003].

[14] Hamamatsu MPPC S13360 series Technical Data Sheet. 2016.02. URL: http://www.hamamatsu.com/resources/pdf/ssd/s13360_series_kapd1052e.pdf.

[15] J. Ninkovic. Silicon photomultiplier developments, 2015. 8th Terascale Detector Workshop 2015, München, Germany. URL: https://indico.desy.de/materialDisplay.py?contribId=1&sessionId=1&materialId=slides&confId=10967.

[16] K. A. Olive et al. (Particle Data Group). Chin. Phys. C,38, 090001 (2014) and 2015 update. URL: http://pdg.lbl.gov/2015/reviews/rpp2015-rev-particle-detectors-accel.pdf.

[17] EJ-200 Plastic Scintillator data sheet. 2016.02. URL: http://fcomp.ist.utl.pt/LRC.web/equipamento/EJ200-datasheet.pdf.

[18] 3M, St. Paul, MN, USA, URL: https://www.3M.com.

[19] Reflector paint technical datasheet, URL: http://www.crystals.saint-gobain.com/sites/imdf.crystals.com/files/documents/sgc-bc620-data-sheet_69725.pdf.

[20] M. Münker, S. Arfaoui, W. Klempt, T. Frisson. Experimental Setup for Characterisation of Scintillator Tiles with SiPM Readout. CLICdp: ECal Lab Meeting (CERN), November 25, 2014. URL: https://indico.cern.ch/event/353737/contribution/2/material/slides/0.pdf.

[21] S. Arfaoui, C. Joram, C. Casella. Characterisation of a Sr-90 based electron monochromator. Technical Report PH-EP-Tech-Note-2015-003, CERN, Geneva, May 2015. URL: https://cds.cern.ch/record/2013995.

[22] OWIS LTM 80M-170 stepper motor technical data sheet. 2016.02. URL: http://www.owis.eu/fileadmin/user_upload/owis.eu/products/pdf/04_Mot_Pos_kapitel_web_01.pdf.

[23] BGA614 Silicon Germanium Broadband MMIC Amplifier Data Sheet. 2016.02. URL: http://www.infineon.com/dgdl/Infineon-BGA614-DS-v02_01-en.pdf?fileId=db3a304314dca3890115418ffd35163a.

[24] PicoScope 6404B technical datasheet. 2016.02. URL: http://ph.rs-online.com/webdocs/1372/0900766b813723a2.pdf.

[25] LABVIEW System Design Software. 2016.02. URL: http://www.ni.com/labview/.

[26] ROOT Data Analysis Framework. 2016.02. URL: https://root.cern.ch.

[27] L. Landau. On the energy loss of fast particles by ionization. *J. Phys.(USSR)*, 8:201–205, 1944.

[28] R. Fruehwirth, H. Pernegger, M. Friedl. Implementation of convoluted Landau and Gaussian Fitting Function in ROOT. 2016.02. URL: https://root.cern.ch/root/html/tutorials/fit/langaus.C.html.

[29] PT1000 thermometer technical datasheet. 2016.02. URL: http://www.farnell.com/datasheets/388391.pdf.

[30] S. Arfaoui. Private communications on Scintillator tiles characterisation for CLIC-ECAL. 2014.

[31] The CALICE collaboration. Electromagnetic response of a highly granular hadronic calorimeter. *Journal of Instrumentation*, 6(04):P04003, 2011. URL: http://stacks.iop.org/1748-0221/6/i=04/a=P04003.

[32] G. Clemens. *Comparison of iron and tungsten absorber structures for an analog hadron calorimeter*. PhD thesis, Hamburg, 2015. Universität Hamburg, Diss., 2015. URL: https://bib-pubdb1.desy.de//record/220093.

[33] The CALICE collaboration. Construction and commissioning of the calice analog hadron calorimeter prototype. *Journal of Instrumentation*, 2010. URL: http://iopscience.iop.org/article/10.1088/1748-0221/5/05/P05004/meta.

[34] F. Simon and C. Soldner. Uniformity studies of scintillator tiles directly coupled to SiPMs for imaging calorimetry. *Nuclear Instruments and Methods in Physics Research Section A: Accelerators, Spectrometers, Detectors and Associated Equipment*, 620(2–3):196 – 201, 2010.

[35] K. Krüger. Recent AHCAL test beam results. CLIC Detector and Physics Collaboration Meeting 30-31 August 2016 CERN. URL: https://indico.cern.ch/event/487219/contributions/2266972/attachments/1328748/1995832/AHCAL_CLICdp_20160830.pdf.